Technical University of Munich
TUM School of Natural Sciences
Particle Physics at Low Energies

Thesis for the Master's degree programme in Nuclear, Particle, and Astrophysics

Pulsed Neutron Beam for Beta Spectroscopy

Gepulster Neutronenstrahl für die Betaspektroskopie

Michael Patrick Gudd

30th May 2025

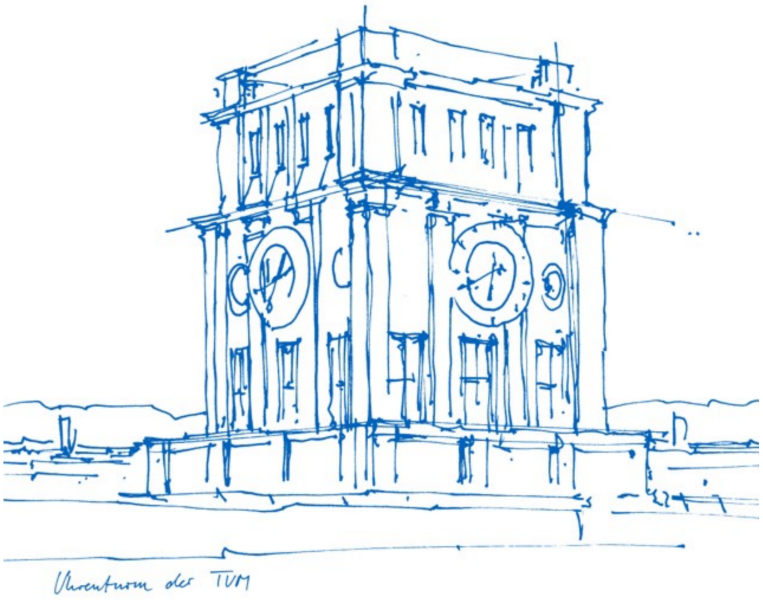

Erstgutachter (Themensteller): Prof. Dr. B. Märkisch
Zweitgutachter: Prof. Dr. P. Fierlinger

Contents

Abstract v

1 Introduction 1

2 Theoretical Foundations and Experiment 3
2.1 Standard Model 3
2.2 Neutron Beta Decay 5
2.3 PERC 8
2.4 The Beta Asymmetry 9

3 Chopper Optimization 11
3.1 Motivation 11
3.2 Disc Chopper 12
3.3 Opening Function 16
3.4 Neutron Absorber 21
3.5 Rotational Energy and Tensile Stress 23
3.6 Background 27

4 Simulation Framework 29
4.1 McStas and McStasScript 29
4.2 Simulation Template 30

5 Neutron Density Optimization 37
5.1 Reduction Effects 37
5.1.1 Reflectivity 37
5.1.2 Broadening 41
5.1.3 Gaps 43
5.1.4 Combination 45
5.2 Optimizations 46
5.2.1 Wavelength 47
5.2.2 Increased Height of Connection Guides 49
5.2.3 Increased Height of PERC Guides 50
5.2.4 Increased Width of PERC Guides 52
5.2.5 Widening of Connection Guides 53

5.2.6 Widening of all Guides 54
5.2.7 Narrowing of Connecting Guide 57
5.2.8 Guide Type 58
5.2.9 No Broadening within PERC 59
5.2.10 Summary 61

6 Performance Estimation 65
6.1 Neutron Pulse 65
6.2 Magnetic Mirror Effect 67
6.3 Decay Rate Estimate 75

7 Conclusion and Outlook 77

A Additional Figures 79

Bibliography 81

Abstract

Since the late 1960s, the Standard Model of Particle Physics has been used to describe most physical processes. However, it cannot describe some observations. The search for non-standard model phenomena is the focus of many current experiments. The study of the beta decay of the free neutron is a great way to test the Standard Model, since the system of observables is overdetermined. The PERC spectrometer, which is the successor to PERKEO III, is designed to observe neutron beta decays in order to determine decay coefficients like the Fierz interference term b and the beta asymmetry parameter A. With A, the ratio of axialvector to vector coupling λ can be determined. In combination with the neutron lifetime τ_n, this enables the calculation of the element V_ud of the Cabibbo-Kobayashi-Maskawa matrix, for which current most precise values show a deviation of the expected unitarity in the first row. b is sensitive to scalar and tensor interactions, which are non-existent in the Standard Model. The goal of PERC is to achieve a precision of these and other decay coefficients, that is up to one order of magnitude better than the existing values from the PERKEO-series. This would make PERC's results world-leading.
Measurements with PERC make use of a pulsed neutron beam to improve systematics. To this end, the geometrical concept for a disc chopper was developed as part of this thesis. This includes the optimization of the chopper with respect to the average event rate, as well as an analysis of the chopper opening function. Furthermore, a thickness of $d = 1\,\mathrm{mm}$ of the absorber material boron carbide was found sufficient for a transmission $T \ll 10^{-5}$ at an average neutron wavelength of $\lambda = 5\,\text{Å}$. Occurring stresses are below 13.9 MPa, ensuring a safe chopper operation at $f_\mathrm{chop} = 50\,\mathrm{Hz}$, for a disc made of boron carbide and reinforced polyimid. A "PERC-template" for neutron simulations in the Python-API McStasScript was created, to study the effects of changes to the beamline on the average neutron density in PERC. Simulations were performed to find possible optimizations in the beamline to increase the number of observed neutron decays. An increase of the height of the connection guide from 60 mm to 80 mm, for instance, would result in an average gain of 13 % in statistics. Additionally, the neutron pulse, including time-of-flight information, was analyzed to determine the effect of the magnetic mirror effect on the asymmetry measurement and to give an estimate of the decay rate in PERC. The relative correction on the beta asymmetry caused by the magnetic mirror effect was found to be $\frac{\Delta A_\mathrm{MM}}{A} = 2 \times 10^{-4}$. The decay rate of a setup without any optimizations at an average neutron wavelength of 5 Å was simulated to be $r_\mathrm{avg,comp} = 110\,\mathrm{s}^{-1}$, which is

similar to PERKEO III. Including all optimizations, this rate could be increased to up to $400\,\mathrm{s}^{-1}$.

Zusammenfassung

Seit den späten 1960er Jahren wird das Standardmodell der Teilchenphysik zur Beschreibung der meisten physikalischen Prozesse verwendet. Eine Reihe von Beobachtungen kann es jedoch nicht beschreiben. Ein Fokus aktueller Experimente liegt auf der Suche nach physikalischen Phänomenen, die nicht durch das Standardmodell erklärt werden können. Die Untersuchung des Betazerfalls des freien Neutrons bietet hervorragende Möglichkeiten, um das Standardmodell zu testen, da das System von Observablen überbestimmt ist. Das PERC Spektrometer, welches der Nachfolger von PERKEO III ist, dient der Betrachtung von Neutronen-Beta-Zerfällen, um Zerfallskoeffizienten wie den Fierz-Interferenzterm b oder den Beta-Asymmetrie Parameter A zu bestimmen. Mit A kann das Verhältnis zwischen Axialvektor- und Vektorkopplung λ bestimmt werden. In Kombination mit der Neutronen-Lebensdauer τ_n ermöglicht dies die Berechnung des Elements V_ud der Cabibbo-Kobayashi-Maskawa-Matrix, für die die derzeit genauesten Werte eine Abweichung von der erwarteten Unitarität in der ersten Zeile zeigen. b hängt von Skalar- und Tensorwechselwirkungen ab, die laut Standardmodell nicht existieren. Das Ziel von PERC ist es, eine Präzision der Zerfallskoeffizienten zu erreichen, die um bis zu eine Größenordnung besser ist als die bestehenden Messungen aus der PERKEO-Reihe. Damit wären die Ergebnisse von PERC weltweit führend.
Messungen mit PERC verwenden einen gepulsten Neutronenstrahl, um die Systematik zu verbessern. Zu diesem Zweck wurde im Rahmen dieser Arbeit das geometrische Konzept für einen Chopper entwickelt. Dazu gehört die Optimierung der Chopperscheibe im Hinblick auf die durchschnittliche Ereignisrate sowie eine Analyse der Chopperöffnungsfunktion. Außerdem wurde eine Dicke von $d = 1\,\mathrm{mm}$ des Absorbermaterials Borcarbid als ausreichend für eine Transmission $T \ll 10^{-5}$ bei einer mittleren Neutronenwellenlänge von $\lambda = 5\,\text{Å}$ befunden. Die auftretenden Spannungen liegen bei unter 13.9 MPa, was einen sicheren Betrieb des Choppers bei einer Rotationsfrequenz von $f_\mathrm{chop} = 50\,\mathrm{Hz}$ gewährleistet, wenn die Scheibe aus Borcarbid und verstärktem Polyimid besteht. Es wurde ein "PERC-Template" für Neutronensimulationen im Python-API McStasScript erstellt, um die Auswirkungen von Änderungen an der Beamline auf die durchschnittliche Neutronendichte in PERC zu untersuchen. Es werden Simulationen durchgeführt, um mögliche Optimierungen an der Beamline zu finden, die die Anzahl der beobachteten Neutronenzerfälle vergrößern. So bei-

spielsweise resultiert eine Erhöhung des Leiters zwischen PERC und dem Selektor von 60 mm auf 80 mm im Durchschnitt in 13 % mehr Neutronenzerfällen. Darüber hinaus wurde der Neutronenpuls, einschließlich der Flugzeitinformationen, analysiert, um den Effekt des magnetischen Spiegeleffekts auf die Asymmetriemessung zu bestimmen und eine Abschätzung der Eventrate in PERC zu erhalten. Die relative Korrektur der Beta-Asymmetrie durch den magnetischen Spiegeleffekt beträgt $\frac{\Delta A_{\mathrm{MM}}}{A} = 2 \times 10^{-4}$. Die Eventrate ohne Betrachtung jeglicher Optimierungen bei einer durchschnittlichen Neutronen-Wellenlänge von 5 Å ergibt $r_{\mathrm{avg,comp}} = 110\,\mathrm{s}^{-1}$, was vergleichbar mit PERKEO III ist. Wenn alle Optimierungen einbezogen werden, ergäbe sich eine Eventrate von bis zu $400\,\mathrm{s}^{-1}$.

Chapter 1

Introduction

In the second half of the 20th century, the Standard Model (SM) of Particle Physics was introduced, combining three of the four know fundamental forces. It includes the electromagnetic, the strong, and the weak interactions in one theory, enabling it to describe most elementary processes. It categorizes the elementary particles in quark pairs, lepton pairs and force carrying bosons. Although it is widely successful, it can not describe some of the observed physical processes and lacks the integration of gravitation. A focus of current experiments is to discover additional non-standard model phenomena.

This thesis starts with a short description of the SM, followed by a review of the β^--decay of the free neutron. With its multitude of decay coefficients, the free neutron decay is overdetermined in the framework of effective field theories and hence a great process to test the SM. Following this, comes an overview of the experimental setup of PERC (Proton and Electron Radiation Channel), which investigates the neutron decay, and how it plans to measure the beta asymmetry A.

The reasons why using a pulsed beam for PERC is beneficial are explained. As the beam coming from the FRM II is continuous, a disc chopper is needed to segment the beam into neutron pulses. In order to increase statistics, the chopper design is optimized to achieve a high average decay rate. Additionally, the neutron absorbing material of the disc is described. To ensure a safe operation, the stresses occurring in the disc and its rotational energy are evaluated.

A neutron simulation template of PERC is developed in McStasScript, that can be used to investigate the pulsed neutron beam. Especially with the cold source of the FRM II being unavailable for the beginning of PERCs' operation, the number of observed neutron decays needs to be maximized. Possibilities to increase the neutron intensity inside the decay volume are evaluated.

The properties of the neutron pulse are used to give a first estimate of the relative correction on the beta asymmetry due to the magnetic mirror effect. Additionally, an

estimate of the average event rate, measured by the downstream detector, is given, before concluding with a short summary and outlook.

Chapter 2

Theoretical Foundations and Experiment

For over half a century, the Standard Model of Particle Physics has been a successful concept to describe fundamental particles and their interactions. However, some observations cannot be explained by it, which motivates searches for physics beyond the Standard Model. This chapter gives a short introduction to the Standard Model and its properties and especially introduces the β^--decay of the free neutron. This process is highly suitable to investigate potential beyond Standard Model physics. Afterwards, an introduction to the spectrometer PERC, currently being set up at the FRM II in Munich is given, for which this thesis provides an optimization of the pulsed neutron beam.

2.1 Standard Model

The Standard Model of Particle Physics (SM) was introduced in the second half of the 20th century. It unifies the electroweak and strong interaction and can hence be used to describe most known particle behaviors. The known elementary particles are grouped into three categories: quarks, leptons and bosons. Matter is formed by quarks and leptons, each occurring in three generations. These twelve particles are called fermions and have a spin of $\frac{1}{2}$. The remaining particles are called bosons, they are the force carrying particles that mediate electroweak and strong interactions between the fermions. All bosons (g, γ, Z^0, W^+, W^-) have spin 1, except for the Higgs-boson H, which has spin 0.

The force carriers for the weak interaction, which is responsible for the free β^--decay of the neutron, are Z^0, W^+ and W^-. The Z^0-boson carries no charge and does not change the flavour of fermions. In contrast, $W^\pm$-bosons are electrically charged and can alter the flavour of fermions in charged-current interactions. The transitions between quarks are described by the Cabibbo-Kobayashi-Maskawa-Matrix V_{CKM} (CKM-matrix) [1]. It is the following unitary 3×3 matrix, which describes the coupling strengths (i.e. transition probabilities) between up- and down-type quarks:

$$V_{CKM} = \begin{pmatrix} V_{\mathrm{ud}} & V_{\mathrm{us}} & V_{\mathrm{ub}} \\ V_{\mathrm{cd}} & V_{\mathrm{cs}} & V_{\mathrm{cb}} \\ V_{\mathrm{td}} & V_{\mathrm{ts}} & V_{\mathrm{tb}} \end{pmatrix}. \tag{2.1}$$

V_{ud} is the probability for a down-quark to change into an up-quark, and similarly for all other entries.

The $W^{\pm}$-bosons couple to the eigenstates of the electroweak interaction $|d'\rangle$, $|s'\rangle$ and $|b'\rangle$. As they are a composition of the mass eigenstates $|d\rangle$, $|s\rangle$ and $|b\rangle$ the mixing is given by

$$\begin{aligned} \begin{pmatrix} |d'\rangle \\ |s'\rangle \\ |b'\rangle \end{pmatrix} = V_{CKM} \begin{pmatrix} |d\rangle \\ |s\rangle \\ |b\rangle \end{pmatrix} &= \begin{pmatrix} V_{\mathrm{ud}} & V_{\mathrm{us}} & V_{\mathrm{ub}} \\ V_{\mathrm{cd}} & V_{\mathrm{cs}} & V_{\mathrm{cb}} \\ V_{\mathrm{td}} & V_{\mathrm{ts}} & V_{\mathrm{tb}} \end{pmatrix} \begin{pmatrix} |d\rangle \\ |s\rangle \\ |b\rangle \end{pmatrix} = \\ &= \begin{pmatrix} 1 - \frac{\lambda^2}{2} & \lambda & A\lambda^3(\rho - i\eta) \\ -\lambda & 1 - \frac{\lambda^2}{2} & A\lambda^2 \\ A\lambda^3(1 - \rho - i\eta) & -A\lambda^2 & 1 \end{pmatrix} \begin{pmatrix} |d\rangle \\ |s\rangle \\ |b\rangle \end{pmatrix}. \end{aligned} \tag{2.2}$$

Here the CKM matrix is parameterized after L. Wolfenstein [2]. λ is the sine of the Cabibbo angle, while A is related to the strength of interactions between the third-generation quarks and lighter quarks. ρ and η determine the complex phase, that ensures the charge-parity-violation (CP-violation).

Limits of the Standard Model

Although the SM is capable of describing the majority of known particle physics phenomena, there are still observations that cannot be understood within its framework.

Important examples that indicate beyond standard model physics are among others the lack of unification of the SM with gravity, neutrino oscillations, observed with experiments like Super-Kamiokande, that require non-zero neutrino masses [3], dark matter [4] or the matter-antimatter asymmetry of the universe, which the SM cannot explain with the existing violations.

All these observations and open questions imply the existence of physics beyond the Standard Model of Particle Physics, motivating extensive searches for non-standard model phenomena with the aim to obtain a more complete theory.

2.2 Neutron Beta Decay

There are mainly two ways to search for beyond SM physics. High-energy and low-energy experiments. High-energy experiments, mainly colliders such as the Large Hadron Collider near Geneva, aim to directly create unknown particles or to induce new processes. They typically utilize energies of GeV upwards. This is backed by the propagator term [5] which is given by

$$G(p) = \frac{i}{q^2 - m^2 + i\epsilon}. \tag{2.3}$$

q is the four-momentum, while m is the mass of the exchanged particle and ϵ is needed to incorporate causality. When $q \approx m$, a resonance effect occurs, enhancing the production probability. However, the accessible energy range is limited as achieving even higher energies becomes increasingly harder. Low-energy instruments focus on states where $q \ll m$. In these cases, heavy particles can only be part of virtual processes and the propagator term can be simplified. Heavy particles nevertheless contribute to the interaction, and although their effects are small, they can be measured as deviations from theoretically expected values. This poses the need of high-precision experiments like PERC. With these, beyond Standard Model physics can be found, without the need of directly creating the corresponding particle. Hence, the low energy spectrum becomes accessible.

The free neutron has a relatively long lifetime of $\tau_\mathrm{n} = 878.4(5)\,\mathrm{s}$ [6], which is part of why the beta decay is an ideal process to investigate low energy physics as the neutron can be transported to the experimental setup, but also has a reasonable decay rate. In β^--decay, a free neutron n decays into a proton p, an electron e^- and an electron-antineutrino $\overline{\nu}_e$ [7].

$$n \rightarrow p + e^- + \bar{\nu}_\mathrm{e} \tag{2.4}$$

This is a three body decay, with an energy release resulting from the difference between initial mass of the neutron and the masses of the decay products. It is given by

$$\Delta E = m_\mathrm{n} - m_\mathrm{p} - m_{e^-}(-m_{\overline{\nu}_e}) = 782\,\mathrm{keV}. \tag{2.5}$$

Within the SM the electron-antineutrino has no mass. The excess energy is translated into kinetic energy of the decay products, with parts of it not being measurable, as the electron-antineutrino cannot be detected in PERC. However, the missing momentum in a detailed analysis proves its existence. The Feynman diagram of the neutron decay is shown in figure 2.1.

The prerequisite for the decay is the conversion of a down-quark into an up-quark.

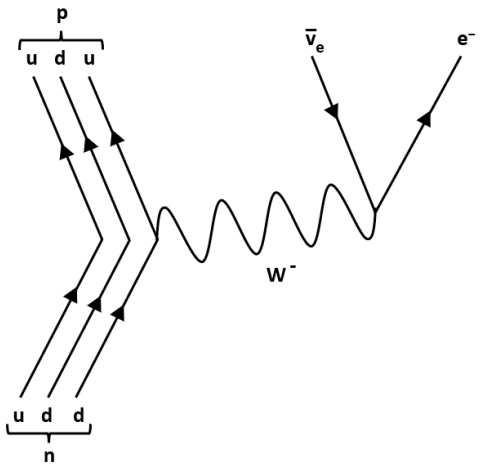

Figure 2.1: Feynman diagram of the free beta decay of a free neutron. A down-quark is converted into an up-quark, thereby releasing a W^--boson. As the boson is an unstable virtual particle, it decays, producing an electron e^- and an electron-antineutrino $\overline{\nu}_e$.

Within the SM, this is fully described by the CKM matrix, especially by V_{ud} and the corresponding parameters in equation (2.2).

To mathematically account for potential non-standard model physics an extended description of the neutron beta decay is needed. Such a description can be achieved by Effective Field Theories (EFTs). Instead of a complete theory, EFTs aim to describe physical processes under specific conditions and in predefined energy ranges. Although this limits their area of application, it enables the description with many degrees of freedom. EFTs are parameterized by so-called Wilson coefficients, which can represent beyond SM physics. One such theory is the weak Effective Field Theory (WEFT), which describes low-energy processes like the neutron beta decay. Using WEFT one can formulate an equation of the differential decay width of the neutron decay, derived by Jackson, Treimann and Wyld [8]. A detailed derivation can be found in [9]. The differential decay width is then given by

$$\begin{aligned} &\mathrm{d}\Gamma_\mathrm{n}(E_\mathrm{e}, \Omega_\mathrm{e}, \Omega_\nu, \langle \boldsymbol{\sigma}_\mathrm{n} \rangle) \mathrm{d}E_\mathrm{e} \mathrm{d}\Omega_e \mathrm{d}\Omega_\nu = \\ &\frac{1}{32\pi^5} \cdot \rho\left(E_\mathrm{e}\right) \xi \cdot \left(1 + a\frac{\boldsymbol{p}_\mathrm{e} \cdot \boldsymbol{p}_\nu}{E_\mathrm{e} E_\nu} + b\frac{m_\mathrm{e}}{E_\mathrm{e}} + \langle \boldsymbol{\sigma}_n \rangle \left[A\frac{\boldsymbol{p}_\mathrm{e}}{E_\mathrm{e}} + B\frac{\boldsymbol{p}_\nu}{E_\nu} + D\frac{\boldsymbol{p}_\mathrm{e} \times \boldsymbol{p}_\nu}{E_\mathrm{e} E_\nu}\right]\right). \end{aligned} \tag{2.6}$$

The equation describes the probabilities of the electron and the antineutrino to have certain energies and directions, including spin dependencies. Thus, it links the neutron beta decay to measurable properties that are accessible in PERC. A is the beta

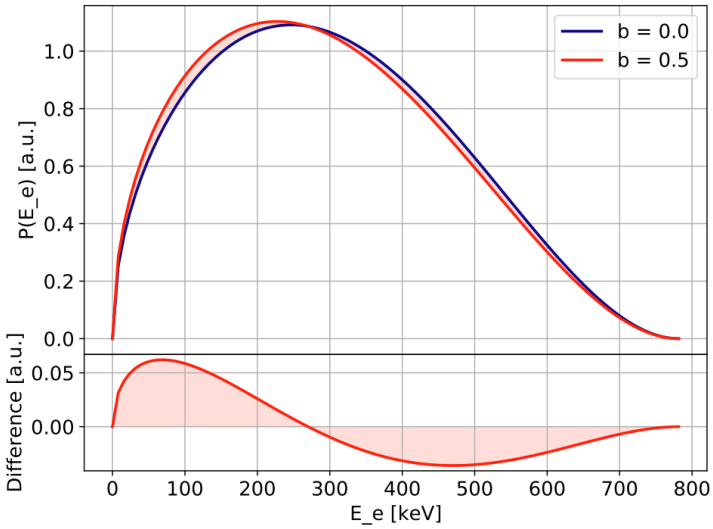

Figure 2.2: Effect of a non-zero Fierz interference term b on the electron beta spectrum. The value of $b = 0.5$ is exaggerated for visualization purposes. Image is taken from [11].

asymmetry and b is the Fierz interference term, which have both been measured by PERKEO III. E_e and E_ν are the energies of the decay particles while p_e and p_ν are the corresponding momenta. The average spin orientation is given through $\langle \boldsymbol{\sigma}_\mathrm{n} \rangle = \frac{\langle \boldsymbol{J} \rangle}{J}$. a, ξ, B and D are additional decay parameters, next to A and b. $\mathrm{d}\Gamma_n$ is the differential decay width and $\rho(E_\mathrm{e})$ is the phase space density.

Within the Standard Model, this expression can also be derived, using Fermi's Golden rule. The derivation can be found in [10]. The resulting differential decay width then depends on only three parameters. On the previously introduced probability V_ud, the ratio between axial-vector coupling and vector-coupling λ and the coupling constant G_F. As the system is hence over-determined, neutron beta decay is an ideal process to look for beyond SM physics. PERC can for example investigate the Fierz interference term, which is zero in the Standard Model as it would introduce scalar and tensor interactions. A non-zero Fierz term would influence the shape of the electron energy spectrum that can be measured with PERC. The effect is visualized in figure 2.2.

2.3 PERC

PERC, which is short for Proton and Electron Radiation Channel, is a high precision spectrometer which is currently set up at the MEPHISTO beam site of the FRM II in Munich. It is the successor of PERKEO III and will primarily measure to determine the decay coefficients A, b and C of the free neutron decay. The aim is to improve the precision of each coefficient by one order of magnitude, compared to existing measurements. In addition, the combination of electron and proton measurements, that PERC will be able to perform, will allow a measurement of the electron-neutrino correlation a and the neutrino asymmetry B to be determined.

A visualization of the PERC spectrometer is shown in figure 2.3. In front of the

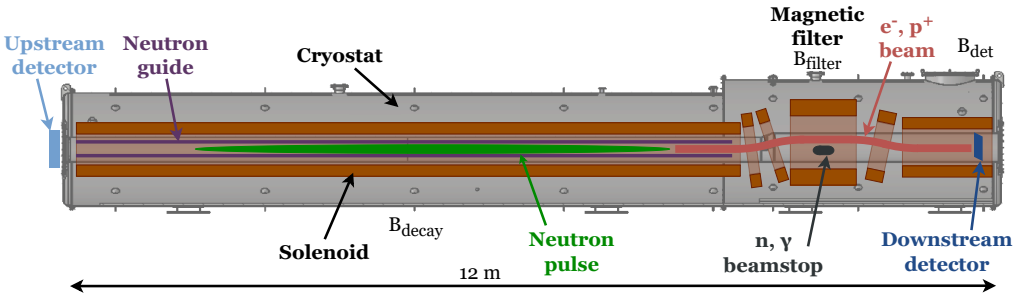

Figure 2.3: Schematic of the PERC spectrometer. The neutrons enter the neutron guide which forms the 8 m long decay volume. This is followed by a gap and then the beamstop, where neutrons that did not decay are absorbed. The charged decay products are guided by the magnetic field to either the downstream detector, if they can pass the magnetic filter, or upstream detector. The neutrons and charged decay particles are decoupled between the neutron guide and the beamstop, by the magnetic field from tilted coils. Image is taken from [9].

spectrometer is a beam line that includes a velocity selector, a chopper and optionally a polarizer to enable measurements of polarized and unpolarized neutron pulses at a known wavelength. The neutrons are coupled into an 8 m long supermirror guide, which, after a gap, is followed by the beamstop, that absorbs the remaining neutrons. The setup is surrounded by a 12 m long superconducting magnet system. This magnet system generates an adjustable magnetic field B_{decay}, between 0.5 T and 1.5 T, which guides the charged decay products of the free neutron decay to the detectors. After the 8 m long neutron guide, the charged decay particles need to be separated from the neutrons. For this, the coils of the magnetic system are tilted in a way that can curve the flight path of the charged particles. In this section, a magnetic filter is implemented as the magnetic field is adjustable between

$B_{\text{filter}} = 3\,\text{T}$ and $B_{\text{filter}} = 6\,\text{T}$. The gradient in the magnetic field causes a magnetic mirror effect for electrons above a critical angle (for details see section 6.2). It follows the downstream detector, which is the main detector, in a magnetic field of up to $B_{\text{det}} = 1\,\text{T}$. The main detector is interchangeable, which allows different setups, like the use of a silicon detector, a magnetic spectrometer, or a plastic scintillator detector. To detect the electrons that have backscattered from the main detector and made it over the filter, there are two upstream detectors positioned on the sides at the entrance of the decay volume. Further information on PERC can be found in [12].

2.4 The Beta Asymmetry

To determine λ, the most sensitive parameter is the beta asymmetry, which, within the Standard Model, can be described by [13]

$$A = -2\frac{|\lambda|^2 + \text{Re}(\lambda)}{1 + 3|\lambda|^2}. \tag{2.7}$$

Due to the asymmetry A, the decay electrons of a polarized neutron beam are not emitted isotropically, but according to a distribution $W(\theta, E_e)$, with θ being the angle between the neutron spin and the electron momentum. For parallel and antiparallel neutron spin alignment, the same solid angle is evaluated by the downstream detector of PERC. As the emission angle θ in the neutron decay is defined by the neutron spin and the electron momentum, the covered emission angles change for parallel and antiparallel alignment. If the neutron spin is parallel to the z-axis, the electron count rate $N^{\uparrow}(E_e)$ for electrons with an emission angle $\theta \in [0, \theta_{\text{crit}}]$ is measured. When the neutron spin is antiparallel, the electron count rate $N^{\downarrow}(E_e)$ includes all emission angles $\theta \in [\pi - \theta_{\text{crit}}, \pi]$. The critical angle θ_{crit} depends on the ratio of $\frac{B_{\text{decay}}}{B_{\text{filter}}}$ and is further discussed in section 6.2. At PERC, the spin of the neutrons can be inversed by a spin flipper. This enables the determination of an experimental beta asymmetry A_{exp}, which is given by

$$A_{\text{exp}}(E_e) = \frac{N^{\uparrow}(E_e) - N^{\downarrow}(E_e)}{N^{\uparrow}(E_e) + N^{\downarrow}(E_e)}. \tag{2.8}$$

PERKEO III was very sensitive to magnetic field inhomogeneities, as critical angles of up to $\theta_{\text{crit}} = 90°$ were considered. With PERC, the magnetic filter decreases the critical angle significantly and the experimental beta asymmetry is described by

$$A_{\text{exp}}(E_e) = \frac{A P_{\text{n}} v_{\text{e}}}{2c}(1 + \cos\theta_{\text{crit}}). \tag{2.9}$$

Where v_{e} is the electron velocity, c is the speed of light and P_{n} is the neutron polarization. The approach with a magnetic filter decreases the count rate, but

amplifies the measured experimental beta asymmetry. Therefore, it decreases the statistical but increases the systematic precision [12]. Equations (2.8) and (2.9) link the beta asymmetry to observables.

Chapter 3

Chopper Optimization

The incoming neutrons from the FRM II form a continuous beam. For the upcoming measurements, this neutron beam should be converted to a pulsed beam to allow for time-of-flight correlations and increased precision on systematics. Therefore, a so-called chopper is needed as part of the beamline before the decay volume. A sketch of the beamline components is shown in figure 4.1. In the following sections, the motivation for a pulsed beam is given. Furthermore, an overview of the chosen method, including timing optimizations, is documented. The resulting chopper opening function is then analyzed and a timing diagram is created to visualize the neutron propagation through PERC. To stop the transmission of neutrons for the desired time period, a neutron absorbing material is needed. The properties and absorption cross section of the chosen material, as well as the absorption process, will be explained. Afterwards, the stored energy and occurring stresses within the component are analyzed. The chapter is then completed by taking a look at further optimization possibilities when reconsidering the background measurement method.

3.1 Motivation

Like its predecessor Perkeo III, PERC aims to use a pulsed beam for operation. Compared to a continuous beam, the use of a pulsed beam has many advantages. Most of these reduce the systematic error as a pulsed neutron beam can provide additional information. First of all, properties can be measured in dependence of the time of flight of the neutrons. The magnetic mirror effect for instance, which will be analyzed in section 6.2, can be measured as a function of time. With time of flight information the settings of the velocity selector can also be verified. Secondly, a period of time can be determined during which all the neutrons in a pulse are within the uniform magnetic field. This enables decay measurements without fringe effects, that would have to be corrected in the data analysis. Thirdly, background measurements can be added to a pulse cycle. With a continuous beam, a shutter positioned before the decay volume has to be closed to enable background measurements. Otherwise, there would always be an overlap of signal and background. This means that experimental properties can change between the measurements of

signal and background. For example thermal drifts might occur in between both measurements. When using a pulsed beam and adding a background measurement to each cycle, both measurements are done under the same conditions. This leads to more accurate results. The same is true for ambient background, such as from surrounding instruments. Furthermore, a pulsed beam has no background caused by the beamstop. Since the measurement of neutron decays is only done while the neutrons are within the uniform decay volume, there are no neutrons hitting the beamstop when the signal is being measured. With a continuous beam, this cannot be realized as there are always neutrons hitting the beamstop. This is especially beneficial as background caused by the beamstop can hardly be measured accurately and has to be approximated or simulated.

However, using a pulsed beam also has disadvantages. The achievable measured decay rate is significantly lower than with a continuous beam as the chopper is closed for the majority of the time, so that no neutrons can enter the decay volume. Furthermore, the decay volume must be sufficiently large to enable reasonable measurement periods. At PERKEO III the combination of both leads to a reduction in measured neutron decays of roughly 90 % compared to a continuous beam. As the uniform decay volume is significantly longer for PERC, the opening angle of the disc will be larger, resulting in a reduction close to 80 %. Additionally, the chopper is a further component that creates background, since it has to be closed during the signal measurement. Due to the layout and inhomogenities of the chopper disc, this background is slightly time-dependent. Therefore, shielding of the component is necessary, as well as an analysis of the background caused by the chopper. Compared to the beamstop, this is easier as it is positioned before the decay volume and can be evaluated with an additional shutter.

3.2 Disc Chopper

There are various types of choppers (fermi chopper, disc chopper,...) that can create a pulsed beam. At PERKEO III a disc chopper was used satisfactorily [14]. PERC will also use this chopper type. A disc chopper is a rotating disc that has a ring made of a neutron absorbing material. This ring covers the whole cross section of the incoming neutron beam. To allow for the transmission of a part of the beam, the ring has one or several windows. A sketch of the disc geometry is shown in figure 3.1. Due to the rotation, this transmission is limited to a certain time period. The disc's geometry and the overlap of such a window with the beam profile as well as the rotation frequency determine the pulse shape. All these parameters need to be optimized to achieve the best possible combination of decay rate and measured time period within PERC.

As explained in section 3.1, a pulsed neutron beam with short pulses that fully fit into the uniform magnetic field is required to enable time-resolved measurements. Moreover, a time span without neutrons passing through the instrument is desired to allow for background measurements. This raises the question of how the time periods should be optimized to achieve this desired state, but also maximizing the number of measured decays. The measured decays correlate with the number of neutron beta decays that occur and the measured time period. The latter is being limited by the available time in which the whole pulse is within the uniform magnetic field. The number of decays increases linearly with the number of neutrons within a single pulse. Since the neutron density is predetermined, the chopper can influence the number of neutrons mainly by the length of the neutron pulse, which is determined by the angular width of the window and the rotation frequency. However, a spatially longer pulse reduces the measuring time as it spends less time completely within the uniform magnetic field. Hence, the optimum between both parameters has to be determined.

First, the ratio of the measurement times for signal and background must be known. This ratio is derived in detail in [15] under the assumption of a fixed total time for measurements $t = t_{\text{meas}} + t_{\text{back}}$. Here, t_{meas} is the time where the combination of signal and background is measured, while t_{back} describes the time period for the background measurement without neutrons in the instrument. In this case t_{meas} is limited, but the optimal ratio remains the same and t can be chosen accordingly. Therefore, the derivation is applicable. The ideal proportionality depends on the rates of signal to background. Since the signal can only be measured in combination with the background, this optimum is described by

$$\left.\frac{t_{\text{meas}}}{t_{\text{back}}}\right|_{\text{opt}} = \sqrt{\frac{R_{\text{sig}} + R_{\text{back}}}{R_{\text{back}}}}. \tag{3.1}$$

R_{sig} and R_{back} are the event rates of signal and background. Compared to PERKEO III, a much better signal to background ratio of $10 : 1$ and above is expected. The following optimizations are based on more conservative numbers of $2 : 1$, for a final design this would need to be reiterated. Hence, t_{back} can be described by the following equation, where χ is a constant used to simplify upcoming calculations

$$t_{\text{back}} = \sqrt{\frac{R_{\text{back}}}{R_{\text{sig}} + R_{\text{back}}}} \cdot t_{\text{meas}} = \sqrt{\frac{1}{3}} \cdot t_{\text{meas}} = \chi t_{\text{meas}} \text{ with } \quad \chi = \sqrt{\frac{R_{\text{back}}}{R_{\text{sig}} + R_{\text{back}}}}. \tag{3.2}$$

This equation requires the time taken to measure the signal t_{meas}. The prerequisite is to only measure within the uniform magnetic field of the decay volume to avoid fringe effects. The uniform decay volume is spatially limited and can be described by

the distances to the chopper disc d_{begin} and d_{end}. Therefore, the available time period where all neutrons are inside the uniform magnetic field is delimited by the time it takes the slowest neutrons to reach the beginning of the volume t_{begin} and the time it takes the fastest neutrons to leave it t_{end}. As the chopper is open for a period of time t_{open}, this time must be subtracted from the available time, as the last neutrons will pass the chopper later, giving the fastest neutrons a head start. A visualization of the distances and time periods is shown in figure A.1. The time period in which the chopper is open is described by the overlap of the angular widths of the chopper window α_{chop} and the neutron beam α_{beam} and the rotation frequency f_{chop}. As long as there is an infinitesimal overlap of both widths, neutrons are transmitted. Hence, the sum of the two angles must be considered, resulting in

$$t_{\text{open}} = \frac{\alpha_{\text{chop}} + \alpha_{\text{beam}}}{2\pi f_{\text{chop}}}. \tag{3.3}$$

This enables an accurate description of the measurement time by

$$t_{\text{meas}} = t_{\text{end}} - t_{\text{begin}} - t_{\text{open}} = \frac{d_{\text{end}}}{v_{\text{max}}} - \frac{d_{\text{begin}}}{v_{\text{min}}} - \frac{\alpha_{\text{chop}} + \alpha_{\text{beam}}}{2\pi f_{\text{chop}}}, \tag{3.4}$$

where v_{min} and v_{max} are the corresponding neutron velocities. These velocities are determined by the velocity selector that only neutrons of certain wavelengths λ can pass. With the use of the de Broglie relation [16], the wavelength can be converted to the velocity of the neutrons:

$$p = \hbar k = mv. \tag{3.5}$$

Using the relation $k = \frac{2\pi}{\lambda}$ and inserting the neutron mass $m_{\text{n}} = 1.674 \times 10^{-27}\,\text{kg}$ and the reduced planck constant $\hbar = 1.054 \times 10^{-34}\,\text{J s}$ [17] leads to

$$\lambda_{\text{n}} v_{\text{n}} = \frac{2\pi\hbar}{m_{\text{n}}} = 3958\,\text{Å}\frac{\text{m}}{\text{s}}. \tag{3.6}$$

At 5 Å the velocity selector delivers $\frac{\Delta\lambda}{\lambda} = 10\,\%$. This gives clearly defined minimum and maximum velocities of $v_{\text{min}} = 720\,\frac{\text{m}}{\text{s}}$ and $v_{\text{max}} = 880\,\frac{\text{m}}{\text{s}}$.

Utilizing the highest possible chopper rotation frequency is desired as this affects the repetition rate for the neutron decay measurements. However, it is limited by three factors. The time between the start of two pulses must cover the time the chopper is open, the time the neutrons take to leave the instrument and then the time for the background measurement. The former and the latter are already defined, while the time it takes the neutrons to leave the instrument can be derived by dividing the length through the neutron velocity of the slowest neutrons. For PERC, the instrument is considered without neutrons when all neutrons that are reflected at

the beamstop reach the exit of the inner guides, the distance between the two being d_{ref}. Therefore, the length a neutron must travel for the instrument to be considered neutron-free, from now on called "attenuation length", is given by $d_{\mathrm{att}} = d_{\mathrm{stop}} + d_{\mathrm{ref}}$, where d_{stop} is the distance between chopper and beamstop. As a result, the highest possible rotation frequency is determined by

$$\begin{aligned} \frac{1}{f_{\mathrm{chop}}} &= t_{\mathrm{open}} + \frac{d_{\mathrm{att}}}{v_{\mathrm{min}}} + \chi t_{\mathrm{meas}} \\ &= \frac{\alpha_{\mathrm{chop}} + \alpha_{\mathrm{beam}}}{2\pi f_{\mathrm{chop}}} + \frac{d_{\mathrm{stop}} + d_{\mathrm{ref}}}{v_{\mathrm{min}}} + \chi \left(\frac{d_{\mathrm{end}}}{v_{\mathrm{max}}} - \frac{d_{\mathrm{begin}}}{v_{\mathrm{min}}} - \frac{\alpha_{\mathrm{chop}} + \alpha_{\mathrm{beam}}}{2\pi f_{\mathrm{chop}}} \right). \end{aligned} \tag{3.7}$$

When introducing an effective length of the decay volume

$$\gamma = \frac{v_{\mathrm{min}}}{v_{\mathrm{max}}} d_{\mathrm{end}} - d_{\mathrm{begin}}, \tag{3.8}$$

the chopper frequency is given by

$$f_{\mathrm{chop}} = v_{\mathrm{min}} \frac{1 - \frac{\alpha_{\mathrm{chop}} + \alpha_{\mathrm{beam}}}{2\pi} (1 - \chi)}{d_{\mathrm{stop}} + d_{\mathrm{ref}} + \chi\gamma}. \tag{3.9}$$

One can see that the only variable that can be freely chosen is the angular width of the chopper opening α_{chop}. All other parameters are already determined by the velocity selector, the magnetic field created by PERC's superconducting magnet or the guide cross sections. Therefore, the measured event rate must be optimized as a function of the opening angle.

The measured event rate is limited by the mean number of decays and the measured time period. The decay rate r can be approximated by dividing the number of neutrons by the mean lifetime of a neutron τ_{n}. Since the number of neutrons per pulse N is given by

$$N = \frac{\alpha_{\mathrm{chop}} \alpha_{\mathrm{beam}}}{4\pi f_{\mathrm{chop}}} (r_{\mathrm{out}}^2 - r_{\mathrm{in}}^2) j, \tag{3.10}$$

where j is the neutron flux density, r_{in} and r_{out} are inner and outer radius of the window [14], the mean decay rate for the measurement is given by

$$\begin{aligned} r &= \frac{N}{\tau_{\mathrm{n}}} t_{\mathrm{meas}} f_{\mathrm{chop}} \\ &= \frac{\alpha_{\mathrm{chop}} \alpha_{\mathrm{beam}}}{4\pi} (r_{\mathrm{out}}^2 - r_{\mathrm{in}}^2) \frac{j}{\tau_{\mathrm{n}}} \left(\frac{d_{\mathrm{end}}}{v_{\mathrm{max}}} - \frac{d_{\mathrm{begin}}}{v_{\mathrm{min}}} - \frac{\alpha_{\mathrm{chop}} + \alpha_{\mathrm{beam}}}{2\pi f_{\mathrm{chop}}} \right). \end{aligned} \tag{3.11}$$

This assumes, that the neutron beam covers the whole height of the window. Using equation (3.9) includes all α_{chop} dependencies, resulting in

$$\begin{aligned} r &= \frac{N}{\tau_{\text{n}}} t_{\text{meas}} f_{\text{chop}} \\ &= \frac{\alpha_{\text{chop}}\alpha_{\text{beam}}}{4\pi}(r_{\text{out}}^2 - r_{\text{in}}^2)\frac{j}{\tau_{\text{n}} v_{\text{min}}}\left(\gamma - \frac{d_{\text{stop}} + d_{\text{ref}} + \chi\gamma}{\frac{2\pi}{\alpha_{\text{chop}}+\alpha_{\text{beam}}} - 1 + \chi}\right). \end{aligned} \tag{3.12}$$

Deriving this with regard to α_{chop} and setting it equal to zero determines the optimal angle. The derivative is

$$\begin{aligned} \frac{dr}{d\alpha_{\text{chop}}} = \frac{\alpha_{\text{beam}}}{4\pi}(r_{\text{out}}^2 - r_{\text{in}}^2)\frac{j}{\tau_{\text{n}} v_{\text{min}}}\Bigg[\gamma - \frac{d_{\text{stop}} + d_{\text{ref}} + \chi\gamma}{\frac{2\pi}{\alpha_{\text{chop}}+\alpha_{\text{beam}}} - 1 + \chi} - \\ - \frac{2\pi\alpha_{\text{chop}}}{(\alpha_{\text{chop}} + \alpha_{\text{beam}})^2} \cdot \frac{d_{\text{stop}} + d_{\text{ref}} + \chi\gamma}{\left(\frac{2\pi}{\alpha_{\text{chop}}+\alpha_{\text{beam}}} - 1 + \chi\right)^2}\Bigg]. \end{aligned} \tag{3.13}$$

In the case where $\chi \neq 1$, the solution is given by

$$\alpha_{\text{chop}} = 2\pi \frac{-1 + \sqrt{1 + \frac{\chi-1}{d_{\text{stop}}+d_{\text{ref}}+\gamma}(\gamma + \frac{\alpha_{\text{beam}}}{2\pi}(d_{\text{stop}} + d_{\text{ref}} + \chi\gamma))}}{\chi - 1} - \alpha_{\text{beam}}. \tag{3.14}$$

Hence, the optimal angular width of the chopper window can be determined. Since $1:1$ signal to background ratio is very unlikely for PERC, a solution for $\chi = 1$ is not part of this thesis. However, it can be found in [14], where d_{stop} would need to be replaced with the attenuation length d_{att}.

3.3 Opening Function

Since the transmitted intensity of the neutron beam depends on the overlap of the chopper window with the incoming neutron beam cross section, a chopper opening function is formed. This opening function depends on the geometry of the neutron beam and the chopper window. To achieve the highest possible stability within the rotating disc, the chopper window has to be sector-shaped. In section 3.2, it was established that the angular width of chopper window and absorber is determined by the ratio between closed and open time periods. Therefore, with a specified height, the geometry of this window is fixed.

The incoming neutron beam before the chopper is rectangular and has a height h, which is the sum of the height of the previous guide and a buffer b to account for an increasing cross section due to divergent neutrons and the gap beforehand (detailed

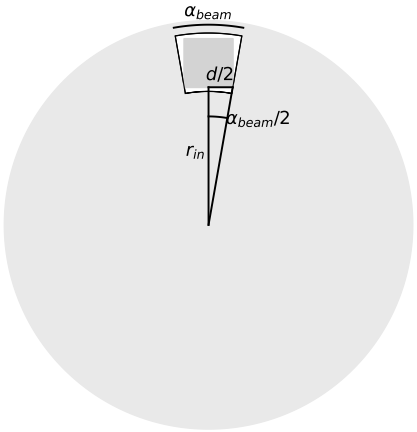

Figure 3.1: Visualization of the geometric determination of angular width of the neutron beam. The angular width is determined with equation (3.15).

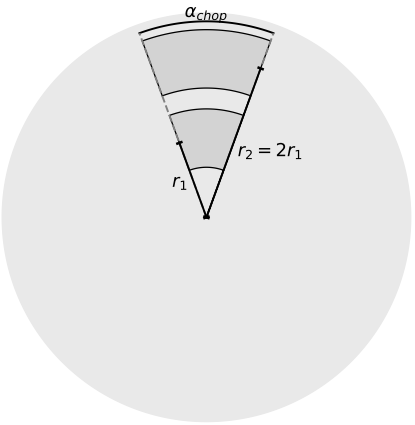

Figure 3.2: Visualization of windows with the same angular width α_{chop} at different radii. At $r_2 = 2r_1$ the resulting window is wider although the angular width is identical.

description in section 5.1.3). The same is true for the width d of the cross section with $d = h$. For simplicity, this geometry is approximated by a sector-shaped cross section as well. The angular width can be determined with basic trigonometry, which is visualized in figure 3.1. The beam angle is then given by

$$\alpha_{\text{chop}} = 2 \arctan\left(\frac{d}{2r_{\text{in}}}\right) = 2 \arctan\left(\frac{d}{2(r_{\text{out}} - h)}\right). \tag{3.15}$$

Here d and h are predetermined by the guide used before the chopper. However, the outer radius of the window can be chosen freely. With the angular approximation, which shall be sufficient for this case, the opening function of the chopper can be approximated by the corresponding ratio of the angular overlap. For $\alpha_{\text{chop}} > \alpha_{\text{beam}}$ this is given by

$$\Phi(\alpha) = \begin{cases} \Phi_0 \cdot \frac{\alpha}{\alpha_{\text{beam}}} & \text{if } \alpha \leq \alpha_{\text{beam}} \\ \Phi_0 & \text{if } \alpha_{\text{beam}} < \alpha < \alpha_{\text{chop}} \\ \Phi_0 \cdot \left(1 - \frac{\alpha - \alpha_{\text{chop}}}{\alpha_{\text{beam}}}\right) & \text{if } \alpha_{\text{chop}} \leq \alpha \leq \alpha_{\text{chop}} + \alpha_{\text{beam}} \\ 0 & \text{else.} \end{cases} \tag{3.16}$$

Φ is a placeholder for physical properties like intensity that correlate with the illuminated area. $\alpha \in [0, 2\pi]$ is the angle between the edge of the window and the y-axis.

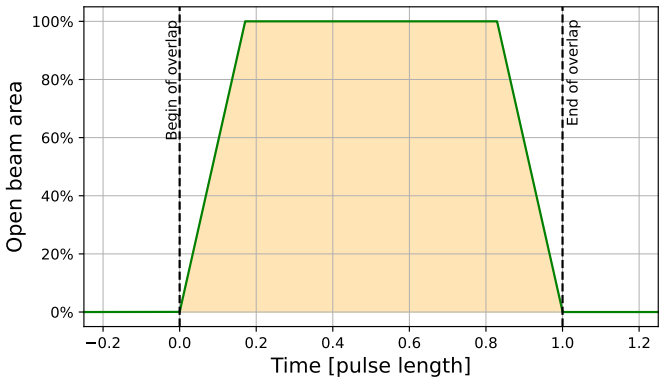

Figure 3.3: Chopper opening function for a 66 mm × 66 mm beam cross section and a disc with an outer radius for the window of 45 cm. The in- and decrease at the beginning and the end of the pulse are caused by an incomplete overlap of the neutron beam cross section with the window.

Therefore, the chopper opening function is characterized by a linear in- and decrease at the beginning and end of the pulse (from now on called "influenced part") and saturates in between when a full overlap is achieved. The width of the influenced part as well as the slope is determined by the beam angle, where a smaller angle is advantageous. Since the beam width is not adaptable, a decrease in angular width can only be achieved by increasing the radius. Figure 3.2 shows windows with the same angular width at different radii. At a larger radius, the distance between both radial edges of the window is also increased, meaning a window of equal size would need a smaller angular width to fit. As a result, it is best to use the largest possible radius. Since the beam height at the FRM II site will be 1.2 m and a chopper housing as well as shielding is needed, the maximum outer radius of the window is assumed to be 45 cm. With a neutron beam cross section of 66 mm × 66 mm including the buffer, the chopper opening function is fully defined. The plot is shown in figure 3.3. As the chopper opening function describes the overlap of the incoming beam cross section with the chopper window, it corresponds to the fraction of neutrons in the beam, that are able to pass the chopper.

With the use of a two-disc chopper, the influenced part could be halved, increasing the slope by a factor of two. A two-disc chopper is based on the same working principle with two counter-rotating discs in a row. The opening process happens in both directions and is therefore twice as fast, resulting in more neutrons within one pulse. However, constructing a two-disc chopper is significantly more complex as the phases need to be stabilized with regard to each other, so that the window

is always at the desired place. Furthermore, two discs are needed, which makes the chopper more expensive. At PERKEO III, the opening function was triangular, hence a two-disc chopper would have had a significant gain of neutrons within one pulse. For PERC on the other hand, the pulse contains 83 % of the neutrons compared to an ideal beam, meaning the gain of a two-disc chopper would roughly be 10 %. It was decided that this is not worth the additional requirements.

An ideal pulse would have a rectangular chopper opening function, with an instantaneous increase of the open area to 100 %. The ratio between the real and the ideal pulse F_{ideal} can be approximated by

$$F_{\text{ideal}} = 1 - \frac{\alpha_{\text{chop}}}{\alpha_{\text{chop}} + \alpha_{\text{beam}}}. \tag{3.17}$$

This ratio is required to calculate the number of neutrons in a neutron pulse, when the average neutron intensity of a continuous beam and the time t_{open} are known.

Now that α_{beam} can be calculated, the findings from section 3.2 can be evaluated with defined parameters. This enables the depiction of a timing diagram, in which the position and time of flight information of the neutron beam with an average wavelength of 5 Å is displayed. This diagram is shown in figure 3.4, a list of the relevant parameters can be found in table 3.1. The table also covers $\lambda = 4.5$ Å and $\lambda = 3$ Å as the wavelength is likely to be adapted (for details see section 5.2.1).

Table 3.1: Input and resulting parameters for the chopper optimization at 5 Å, 4.5 Å and 3 Å. The distances are measured to the chopper disc. As the design of the chopper is not yet final, the distances might change slightly.

Input Parameters					
Average neutron wavelength	λ	5 Å	4.5 Å	3 Å	3 Å
Wavelength resolution	$\frac{\Delta\lambda}{\lambda}$	10 %	10 %	10 %	20 %
Window height	h	60 mm	60 mm	60 mm	60 mm
Window width	d	60 mm	60 mm	60 mm	60 mm
Buffer in height and width	b	6 mm	6 mm	6 mm	6 mm
Outer radius of window	r_{out}	450 mm	450 mm	450 mm	450 mm
Distance begin uniform B-field	d_{begin}	2.41 m	2.41 m	2.41 m	2.41 m
Distance end uniform B-field	d_{end}	8.41 m	8.41 m	8.41 m	8.41 m
Distance beamstop	d_{stop}	10.21 m	10.21 m	10.21 m	10.21 m
Distance reflection	d_{ref}	0.8 m	0.8 m	0.8 m	0.8 m
Rate ratio	χ	$\sqrt{\frac{1}{3}}$	$\sqrt{\frac{1}{3}}$	$\sqrt{\frac{1}{3}}$	$\sqrt{\frac{1}{3}}$
Resulting Parameters					
Minimal neutron velocity	v_{min}	720 $\frac{\text{m}}{\text{s}}$	800 $\frac{\text{m}}{\text{s}}$	1199 $\frac{\text{m}}{\text{s}}$	1099 $\frac{\text{m}}{\text{s}}$
Maximal neutron velocity	v_{max}	880 $\frac{\text{m}}{\text{s}}$	977 $\frac{\text{m}}{\text{s}}$	1465 $\frac{\text{m}}{\text{s}}$	1648 $\frac{\text{m}}{\text{s}}$
Angular width beam	α_{beam}	9.8°	9.8°	9.8°	9.8°
Angular width chopper window	α_{chop}	48.5°	48.5°	48.5°	36.4°
Frequency chopper	f_{chop}	49.3 Hz	54.8 Hz	82.2 Hz	80.8 Hz
Ratio to ideal beam	F_{ideal}	83 %	83 %	83 %	79 %
Time chopper open	t_{open}	3.28 ms	2.95 ms	1.97 ms	1.59 ms
Time signal measurement	t_{meas}	2.92 ms	2.63 ms	1.76 ms	1.32 ms
Time background measurement	t_{back}	1.69 ms	1.52 ms	1.01 ms	0.76 ms

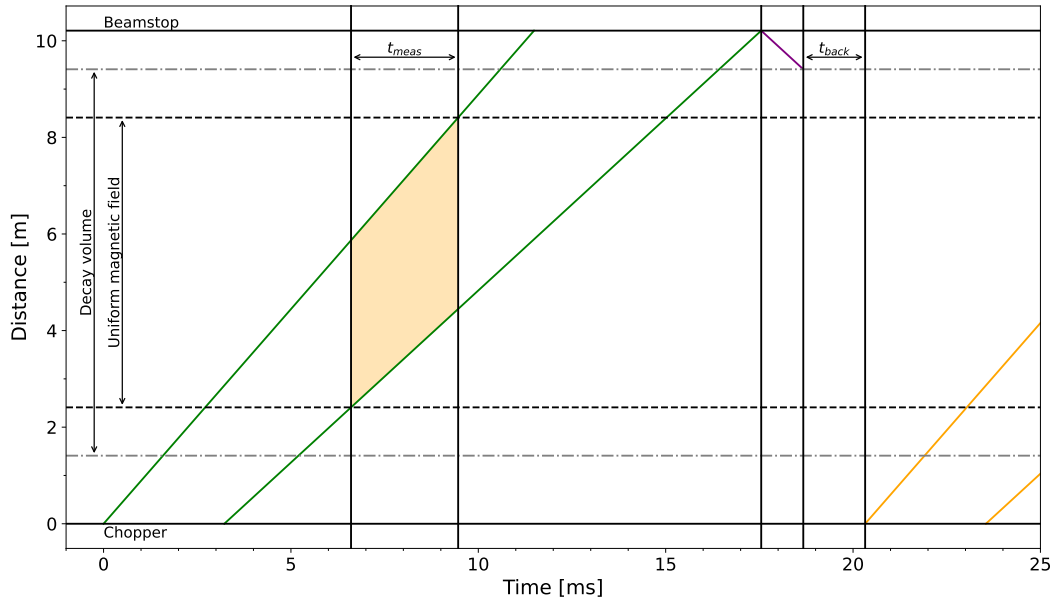

Figure 3.4: Timing diagram of a neutron pulse with $\lambda = 5\,\text{Å}$ moving through PERC, starting at the chopper. The green lines delimit the neutron pulse in position and time. The time period for the signal measurement is highlighted. After the reflected neutrons, shown in purple, reach the decay volume, the instrument is considered neutron-free and the background can be measured. The orange lines show the following pulse.

3.4 Neutron Absorber

For the chopper disc to only be permeable in the designed window, a ring of neutron absorbing material must be placed on the disc. Furthermore, it has to be able to withstand the mechanical forces induced by the fast rotation around its own axis. A couple of different materials like gadolinium, aluminum diboride or lithium fluoride are viable options to absorb neutrons. However, for this chopper disc boron carbide will be used. One of its biggest upsides compared to the other materials is its better availability resulting in a lower price. Boron carbide (B_4C) contains ^{10}B, which captures a neutron [18] as follows

$$^{10}\text{B} + \text{n} \longrightarrow {}^{7}\text{Li}^{\star} + \alpha \longrightarrow {}^{7}\text{Li} + \alpha + 478\,\text{keV}. \tag{3.18}$$

In PERKEO III, the emitted γ background from boron carbide would have been problematic since the detector vessel was positioned right above the chopper. Fortunately, shielding the γ background is no issue with the new PERC setup allowing the use

of boron carbide. Moreover, boron carbide does not emit fast neutrons like lithium fluoride, which would increase requirements for shielding. To calculate the effective absorption cross section for the neutrons reaching the chopper, it is necessary to consider the real velocity of the incoming neutrons as well as the mass fraction of boron in boron carbide. The latter can be calculated with the formula for composite cross sections [19]

$$\sigma_{\mathrm{tot}} = \sum_i Q_{\mathrm{i}} \sigma_{\mathrm{i}}. \tag{3.19}$$

Q_{i} is the weight percentage of nuclei i, while σ_{i} is the corresponding cross section. The sum must be formed over all nuclides i. The same equation can be used to calculate cross sections of isotope mixtures like boron by replacing the weight percentages Q_{i} with the isotope percentages P_{i}. Natural boron contains $\sim 19\,\%$ of ^{10}B, the rest being ^{11}B. While ^{10}B has a neutron absorption cross section of 3835 barn, the isotope ^{11}B has an absorption cross section close to zero [20]. Therefore, using enriched boron carbide $^{10}B_4C$ is advantageous to achieve an up to five times higher absorption cross section.

The listed cross sections from literature apply for neutrons with a wavelength of $\lambda_{\mathrm{lit}} = 1.798\,\text{Å}$. Incoming neutrons at PERC have higher wavelengths in the range of 4.5 Å to 5.5 Å. They are therefore slower and hence more likely to be absorbed. To account for that difference, the $1/v$-law [21] is used. In combination with equation (3.6), it can be simplified to following expression

$$\sigma(\lambda) = \sigma_{\mathrm{lit}} \frac{\lambda}{\lambda_{\mathrm{lit}}}. \tag{3.20}$$

Combining equation (3.20) and (3.19) leads to the effective absorption cross section of boron carbide for the incoming neutrons

$$\sigma_{^{10}\mathrm{B_4C}} = \left((1 - Q_{\mathrm{B}})\sigma_C + Q_{\mathrm{B}}(P_{^{10}\mathrm{B}}\sigma_{^{10}\mathrm{B}} + P_{^{11}\mathrm{B}}\sigma_{^{11}\mathrm{B}})\right) \frac{\lambda}{\lambda_{\mathrm{lit}}}. \tag{3.21}$$

For an average wavelength of 5 Å, a ^{10}B-enrichment of 95 % and the weight percentage $Q_{\mathrm{B}} = 78.28\,\%$, the resulting effective microscopic absorption cross section is 7932 barn.

It is known that the intensity after a penetration depth x can be calculated if the number of particles n, the initial intensity I_0 and the cross section is known. Here, the number of particles can be expressed using the density of the material ρ, the molecular weight M and the Avogadro constant N_{A}. This leads to the following equation

$$I(x) = I_0 \exp(-n\sigma x) = I_0 \exp\left(-\frac{\rho N_{\mathrm{A}} \sigma}{M} x\right). \tag{3.22}$$

From this follows, that the transmission $T(x) = \frac{I(x)}{I_0}$ is strongly dependent on the properties of the chosen material. For the setup at PERC, a transmission $T \ll 10^{-5}$ behind the disc is needed. Obviously, the transmission depends on the level on enrichment of ^{10}B, the density of the material as well as the thickness of the absorber d. This varies from manufacturer to manufacturer. Using the properties from an existing offer, the selected material will have an enrichment greater than 95 % and a density of 2.2 $\frac{\mathrm{g}}{\mathrm{cm}^3}$ to 2.3 $\frac{\mathrm{g}}{\mathrm{cm}^3}$. With a thickness $d = 1\,\mathrm{mm}$, the average transmission $T(d)$ is 5.49×10^{-9} and therefore far below the requirement.

3.5 Rotational Energy and Tensile Stress

The chopper must meet certain safety requirements to be approved for use at the beam site. These include knowledge of the energy content and tensile stress to ensure that the material can withstand the loads. Due to the rotation of the chopper disc around a fixed point, rotational energy is stored within the component. For instance, if the tensile strength is below the tensile stress, this would cause the destruction of the disc, which would cause the disc's stored energy to be released in an explosion-like fashion. Therefore, the rotational energy E_{rot} of the chopper disc must be determined. The rotational energy is given by

$$E_{\mathrm{rot}} = \frac{1}{2} I \omega^2 = 2\pi^2 I f^2. \tag{3.23}$$

f is the rotation frequency, here equal to f_{chop}. I is the moment of inertia, which is determined by the mass distribution in regard to the rotating axis and can be calculated with

$$I = \int_V \boldsymbol{r}_\perp \rho(\boldsymbol{r}) dV, \tag{3.24}$$

where $\boldsymbol{r}_\perp$ is the perpendicular radius to the rotation axis and ρ is the density [22]. The chopper disc can be approximated as a disc with two additional rings of different constant density, since the inner disc and the outer ring are made of the base material, while the neutron absorbing part forms another ring. The additivity of definite integrals allows one to split the integral over the whole radius into a sum of three integrals over each part. Combining this with the moment of inertia for cylinders and hollow cylinders around the z-axis, $I_{\mathrm{cyl}} = \frac{mr^2}{2}$ and $I_{\text{h-cyl}} = \frac{m(r_{\mathrm{in}}^2 + r_{\mathrm{out}}^2)}{2}$, leads to

$$\begin{aligned} &E_{\mathrm{rot}} = \\ &= \pi^3 f_{\mathrm{chop}}^2 \left(d_{\mathrm{b}} \rho_{\mathrm{b}} (r_{\mathrm{in}}^4 + r_{\mathrm{ges}}^4 - r_{\mathrm{out}}^4) + (r_{\mathrm{out}}^4 - r_{\mathrm{in}}^4) \cdot ((d_{\mathrm{b}} - d_{\mathrm{abs}}) \rho_{\mathrm{b}} + d_{\mathrm{abs}} \rho_{\mathrm{abs}}) \right). \end{aligned} \tag{3.25}$$

r_{ges} is the radius of the whole disc including the ring following the neutron absorber, r_{out} and r_{in} are the radii of the window. d_{b} and d_{abs} are thicknesses of the disc and

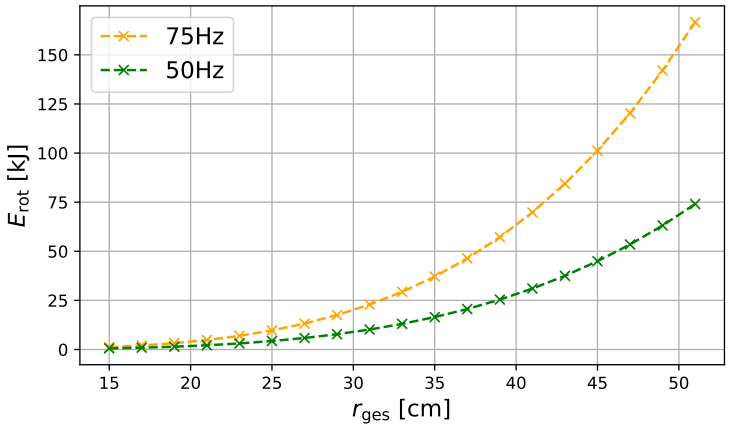

Figure 3.5: Rotational energy for varying disc radii. The green line shows the energy at the operating frequency. The orange line is at +50 % frequency, which is assumed to be the testing frequency for approval.

the neutron absorbing material, while ρ_{b} and ρ_{abs} are their corresponding densities. A plot of the different rotational energies at varying radii is shown in figure 3.5. The calculations assume a 3 cm distance between the outer radius of the window and the disc radius. Furthermore, the thickness of the absorber is 1 mm and its density is $2.3\,\frac{\text{g}}{\text{cm}^3}$. The density for the base material is a rough estimate at $1.4\,\frac{\text{g}}{\text{cm}^3}$, which is a common value for polyimides [23]. For approval, the test rotation frequency is assumed to be 50 % higher than the operating frequency. Hence the figure shows both frequencies. At the desired radius of $r_{\text{ges}} = 48\,\text{cm}$ the rotational energy at 50 Hz is 58 kJ.

The tensile stress is more complex to derive. When a disc is spinning at a constant velocity, each material particle on this disc is subjected to a centripetal acceleration $a_{\text{cp}} = -r\omega^2$, which holds the particle on its circular path. This causes an inertial force resulting in radial and tangential stresses within the disc, visualized in figure 3.6. These stresses can be derived, but as the derivation is lengthy, it is only dealt with in abbreviated form in this thesis. The detailed derivation can be found in [24]. In summary, to determine the stresses, the equation of motion, which is given by

$$\frac{\partial \sigma_{\text{rr}}}{\partial r} + \frac{1}{r}(\sigma_{\text{rr}} - \sigma_{\theta\theta}) = -\rho r \omega^2, \tag{3.26}$$

has to be combined with strain-displacement relations and the plane stress Hooke's law, which results in a differential equation. With the boundary conditions of finite stress at the center and zero radial stress at the edge $\sigma_{\text{rr}}(r_{\text{ges}}) = 0$, this results in the

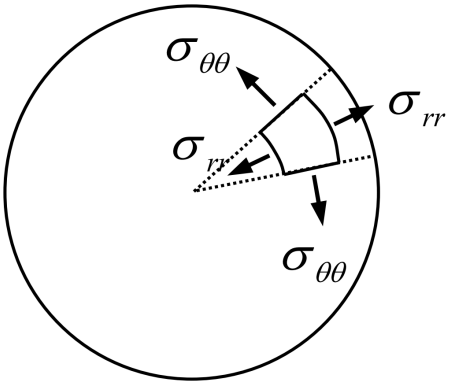

Figure 3.6: Tangential and radial stresses within a rotating disc. Image is taken from [24].

following expressions

$$\begin{aligned} \sigma_{\mathrm{rr}}(r) &= \frac{3+\nu}{8}\rho\omega^2\left(r_{\mathrm{ges}}^2 - r^2\right) \\ \sigma_{\theta\theta}(r) &= \frac{3+\nu}{8}\rho\omega^2\left(r_{\mathrm{ges}}^2 - \frac{1+\nu}{3+\nu}r^2\right). \end{aligned} \tag{3.27}$$

ν is the material specific Poisson's ratio, which defines the ratio between transverse and axial strain. In figure 3.7, an example for the radius-dependent stresses in a chopper disc with $r_{\mathrm{out}} = 45\,\mathrm{cm}$ is shown. It can be seen that the highest occurring stresses are in the center with the tangential and radial stress being equal. Therefore, a plot for the maximum occurring tensile stresses for different radii can be created by considering $r = 0$. The result is shown in figure 3.8.

Boron carbide has a tensile strength of approximately 220 MPa. For polyimides, which are likely to be used as base disc material, the tensile strength ranges from 100 MPa to 300 MPa for reinforced polyimides. At the desired radius of $r_{\mathrm{ges}} = 48\,\mathrm{cm}$, the maximum stresses at the operating frequency are 13.9 MPa, which is far below the maximum tensile strength. Therefore, the desired radius should be possible, with the only limitations coming from the test requirements for approval. With the common safety factor of 4, it should even be possible to withstand a test at +50 % frequency when the right polyimid is chosen.

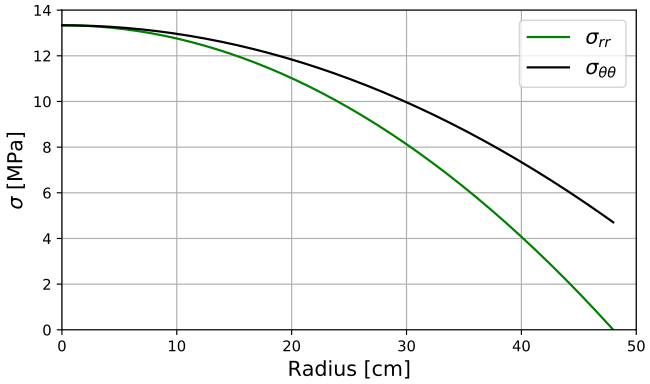

Figure 3.7: Stress curves for a disc chopper with $r_{\text{out}} = 45\,\text{cm}$ at a frequency of 50 Hz with a Poisson's ratio of 0.4. Maximum stresses occur at $r = 0$.

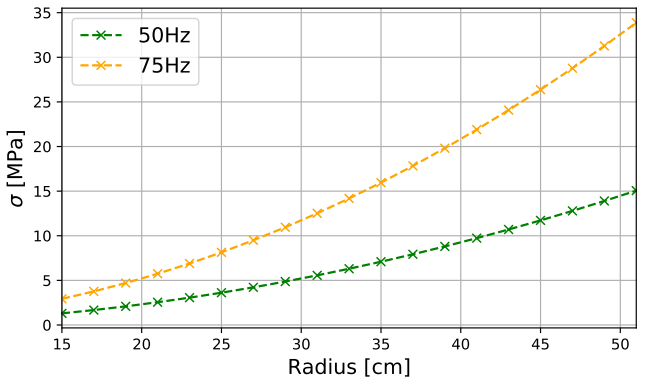

Figure 3.8: Maximum stress for varying radii. The green line shows stresses at the operating frequency, while the orange line shows the stress at the expected testing frequency. Both curves are far below the tensile strength of the desired materials.

3.6 Background

Currently the conditions to measure the background are chosen very conservative. This has a strong effect on the chopper's rotation frequency, which is equivalent to the repetition rate of the signal measurement. A first possible optimization is to reevaluate the signal to background rate. With PERC, it is assumed that it should be sufficient to only measure the background for a time period of 0.5 ms. Compared to the current analysis, this would save 1.2 ms per cycle. Furthermore, the definition when the instrument is neutron-free could be changed. As only a small fraction of the neutrons will be reflected, it could be said that the background can be measured as soon as the last neutrons hit the beam stop. Combining both would increase the measured neutron decays in a given time period by approximately 12 %.

The positioning of PERC also opens up the discussion whether the background needs to be measured after every pulse. The detectors will be far away from other experiments with good shielding possibilities. Therefore, the dominant background would come from the experimental setup itself. Such a background is relative constant and could occasionally be measured separately. Doing background measurements separately massively reduces the time between chopper openings as the instrument never has to be neutron-free. Hence, a consecutive pulse could be timed in a way that it reaches the uniform magnetic field as soon as the last neutrons of the previous pulse are absorbed by the beamstop. A visualization of this approach is shown in figure 3.9. The highest possible frequency is then given by

$$f_{\text{chop}} = (t_{\text{stop}} - t_{\text{begin}})^{-1} = \left(\frac{d_{\text{stop}} - d_{\text{begin}}}{v_{\text{min}}} \right)^{-1} . \tag{3.28}$$

At 5 Å this would mean a chopper frequency of 91 Hz, which would increase statistics by almost 86 %.

Increasing the frequency in this fashion has a massive impact on the rotational energy and occurring stresses. As one can see in equations 3.25 and 3.27, both properties are proportional to the frequency squared. With the desired radius, this will make it impossible to authorize operation as the stresses will be much closer to the maximum tensile strengths. Therefore, a two-window chopper disc should be considered. This halves the rotation frequency as well as the available angular width of the window. Hence there is a trade-off between chopper frequency and the chopper opening function. As a result, the number of neutrons within one pulse decreases. Overall, this would still increase statistics massively due to the higher repetition rate, at the expense of the background not being measured after each pulse.

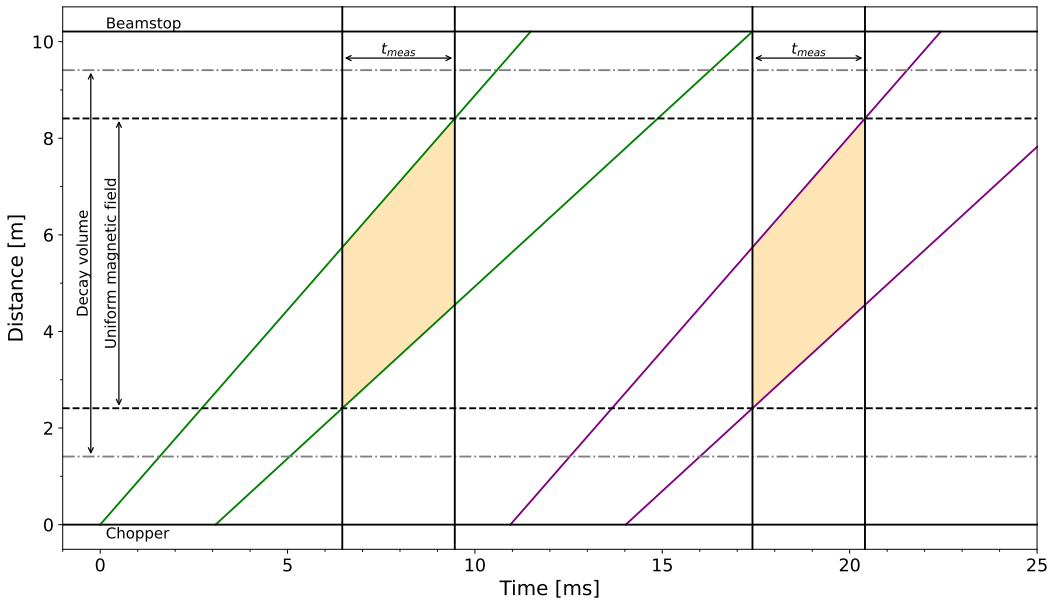

Figure 3.9: Timing diagram for a setup without active background measurement. The neutrons have an average wavelength of 5 Å. The following pulse can start earlier, which increases statistics due to a higher repetition rate.

Chapter 4

Simulation Framework

For the design and optimization of PERC and its surrounding components, simulations in different areas are essential. The optimization of the pulsed neutron beam is one important part of these. This chapter explains the used tools for a comprehensive simulation setup of the pulsed neutron beam. Additionally, the build up of a "PERC-template", with a detailed overview of components and technical specifications, for neutron simulations is described. Assumptions and limitations are considered and a brief introduction to the unit test and verification is given.

4.1 McStas and McStasScript

Simulations are an essential part of understanding the underlying physical effects of experiments and optimizing setups. The leading tool for neutron-optical simulations is the Monte-Carlo simulation software McStas. McStas is a meta-language based in C, which allows to build complete experimental setups using pre-configured components such as velocity selectors or supermirrors. It also enables the inclusion of self-written components, making it very versatile.

McStas is a quasi-Monte-Carlo technique that relies on the law of large numbers. This law concerns the behaviour of sums of large numbers of random variables. It states that the sum of function values for random numbers divided by the number of values n converges to the expectation of the function if that function is integrable and finite [25]. So as n becomes very large,

$$\frac{1}{n}\sum_{i=n} f(u_\mathrm{i}) \rightarrow \frac{1}{b-a}\int_a^b f(u)du, \tag{4.1}$$

where a and b are the borders of the interval. In this case, it means that a large number of neutrons is generated and simulated, while absorption, reflection and transmission are taken into consideration. Each neutron carries information about properties such as energy or divergence. All neutrons are evaluated, so parameters converge to the expectation value and simulated results can be obtained.

Since Monte-Carlo simulations are computationally expensive, McStas assigns each neutron a weight factor [26]. This weight factor represents the probability of a neutron's existence at a certain point in space and time. So if a neutron is reflected with a probability of 10 %, the weight factor is reduced to $\frac{1}{10}$ of the previous weight. This way, only a fraction of the neutrons for a fully realistic simulation needs to be simulated, as it would require ten simulated neutrons for each reflected neutron to form the average. Each weight factor is adjusted after an interaction or after a component. As a result, runtimes are massively reduced.

With McStasScript, a Python-API has been developed that allows, for instance, the integration of McStas simulations in jupyter notebooks. This reduces the time and effort required for data analyses as they can be implemented in the same tool. McStasScript is also accessible to a wider group of students, as Python is now more common than C within that audience. The user creates an instrument object within Python, which then generates an instrument file in C, which performs the simulation [27].

As the working group had no experience with McStasScript, part of this thesis was to pioneer and test its possibilities. For the upcoming simulations, McStas version 3.4 and McStasScript version 0.0.66 were used.

4.2 Simulation Template

Simulations can only be trusted to a limited extent. While in most cases assumptions have to be made to simplify the setup, a major issue with simulations is ensuring high accuracy within the setup and data. Additionally, validating simulations is very time-consuming. The use of a template is therefore advantageous as it only needs to be validated once and can then be used as a foundation. Furthermore, it significantly increases efficiency. Customizations are compatible with existing simulations and can be implemented quickly, while also ensuring that parameters are consistent across simulations. Therefore, one target of this thesis was the creation of a template describing the experimental setup of PERC.

Within his thesis, A. Hollering analyzed the "SR-4b" guide (from now on called "MEPHISTO guide"), which transport the neutrons from the reactor to the neutron guide hall east at the FRM II to the beam site called "MEPHISTO" [28]. With the insight of those simulations, he created a component file for McStas, which was later optimized by B.Märkisch. This file is the starting point of my template as it can be used as a source, which saves the simulation of 45 m of guides in the beginning, thus reducing the computation time considerably. The source has a cross section of 60 mm × 106 mm and can describe a cold and a thermal spectrum. With the

Table 4.1: Technical specifications of the velocity selector for a neutron wavelength of 5 Å [31].

Blade length	250 mm
Blade width	0.4 mm
Number of blades	72
Total length of selector	340 mm
Torsion angle	48.27°
Window width	150 mm
Window height	65 mm
Frequency	424 Hz
Component rotation angle	90°

MEPHISTO guide being made of nickel-titanium supermirrors with $m = 2.5$, the transported neutrons have a divergence of up to 1.25° at a wavelength of 5 Å. Due to the guides creating a curved trajectory to prevent direct view into the reactor, the intensity profile in x-direction is not uniform. Detailed plots of this and the divergence spectrum can be found in [28]. Note that the source is based on simulations as no measurements of the actual neutron spectrum at the beamsite could be performed yet. Therefore, the source can deviate by 20 % or more, making the simulations systematically limited [29].

The source is then followed by a 5 mm gap before the velocity selector begins. The Dornier velocity selector, which has already been used within the PERKEO-series, is described by a component named "Selector". It is a rotating drum with angled neutron absorbing lamellae. Choosing a certain rotation frequency provides an undisturbed path for neutrons of the desired wavelength. Detailed information about the working principle of the velocity selector can be found in [30]. The technical specifications are listed in table 4.1. With the selector window of 150 mm × 65 mm, the overlap with the MEPHISTO guide (60 mm × 106 mm) is unfavorable. While the width cannot be utilized, there would be a cut-off in height. To address this problem, the window can be rotated by 90°, which allows to match the orientation of the window to the guide. This rotation is also taken into account in this template to accurately describe the opening window.

The velocity selector is then followed by a 3 cm gap, before the neutron beam enters a copper-titanium guide. This guide is represented by the component "Guide_gravity". By selecting the value G, one can choose whether gravity should be simulated or not. In upcoming simulations it is set to zero as an analysis has shown that the effect is negligible. Furthermore waviness, which is not yet implemented, can be simulated. The guide is 4 m long with a cross section of 60 mm × 60 mm. The reflectivity para-

Table 4.2: Specifications of the V-bender configured in the simulation template. The reflectivity parameters are explained in section 5.1.1.

Geometry	
Gap to guides	0.03 m
Length single stack	25 mm
Gap between stacks	10 mm
Stack width	80 mm
Stack height	80 mm
Rotation angle	1°
Number of layers	440
Layer thickness	1.82×10^{-6} m
Reflectivity Parameters	
m	6.56
R_0	0.989
α	4.93
W	1.41×10^{-3}
Q_C	0.0102

meters used for this and all following copper-titanium guides are listed in table 5.1. After the guide follows a gap of 3 cm.

Then, a polarizer is needed to enable measurements with polarized neutrons. The polarizer will be based on polarizing supermirrors, but the exact type is still in discussion. While building the template, the usage of a V-bender configuration as proposed in [32] was desired. In simplified terms, a V-bender consists of two alternating stacks of absorbing and spin dependent reflecting layers of material. These stacks are tilted by an angle γ_v against each other to prevent direct view through the polarizer and force at least one reflection. Within the template, this is realized by two "Guide_channeled"-components with the parameters listed in table 4.2.

To account for alignment inaccuracies, the offset angle between the two stacks is usually chosen to be slightly above the optimal angle. As a result, the outgoing neutron beam is not only shifted parallel, but also at an angle to the incoming beam. Without a rotation of PERC's axis, this would result in the neutron beam shifting from side to side within PERC. Hence the setup must be adjusted accordingly. This is considered by rotating the axis along which all following components are orientated. This angle can be chosen freely within the parameter section. Furthermore, it is possible to select whether the polarizer is to be included or not. If it is deactivated, a copper-titanium guide will take its place. In either case follows a 3 cm gap and a copper-titanium guide of 5 m length, with 60 mm × 60 mm cross section,

Table 4.3: Specifications of the chopper configured in the simulation template.

Frequency	47.3 Hz
Radius to outer edge	45 cm
Slit height	67.5 mm
Opening Angle	55.7°
Number of slits	1

connecting polarizer and chopper. At present, it is very unlikely that a V-bender polarizer will be used, so the type of polarizer, its position and therefore the lengths of the surrounding guides will need to be adjusted down the line.

To enable representative time of flight analyses, the continuous beam must be converted to a pulsed beam. This is done using the McStas component "DiskChopper". Similar to the concept explained in section 3.2, it is a one disc chopper. One or multiple openings with adjustable height and an angular width θ are configurable. The beam axis is automatically aligned in the center of the slit opening. A setting can be chosen that allows all simulated neutrons to pass the chopper, by randomly modifying their time to a time where the neutron would not be absorbed. This decreases simulation times when evaluating behind the chopper as neutrons that would get absorbed by the disc are modified to pass. The flux is adjusted accordingly. Neutrons that are not within the chopper geometry are absorbed by default. The used parameters are listed in table 4.3.

On either side, a 3 cm gap separates the chopper from the copper-titanium guides. Since the vacuum chamber for the backscatter detectors prevents the chopper from being closer to the inner guides of PERC, an additional guide has to follow the chopper. This guide is once again made of Cu/Ti supermirrors, has a 60 mm × 60 mm cross section and a length of 45.5 cm. The guide should be as long as possible while still allowing the electrons to reach the backscatter detectors. It is used to minimize gap losses by shortening the free flight path between chopper and the beginning of the inner guides in PERC.

Then follows a gap of 85 cm until the decay volume of PERC begins. The decay volume consists of four 2 m long guides that are placed directly behind each other. To fulfill vacuum requirements [33], each guide has a 2 cm slit on both vertical sides. These slits are positioned at the end of each of the first three guides and will from now on be called "pump slits". The last guide does not need these slits as it has an open end. In order to not lose any neutrons in these slits, the concept includes a 2 mm broadening of the consecutive guide. This increases the cross section from 60 mm × 60 mm at the entrance to 66 mm × 60 mm at the end of the decay volume.

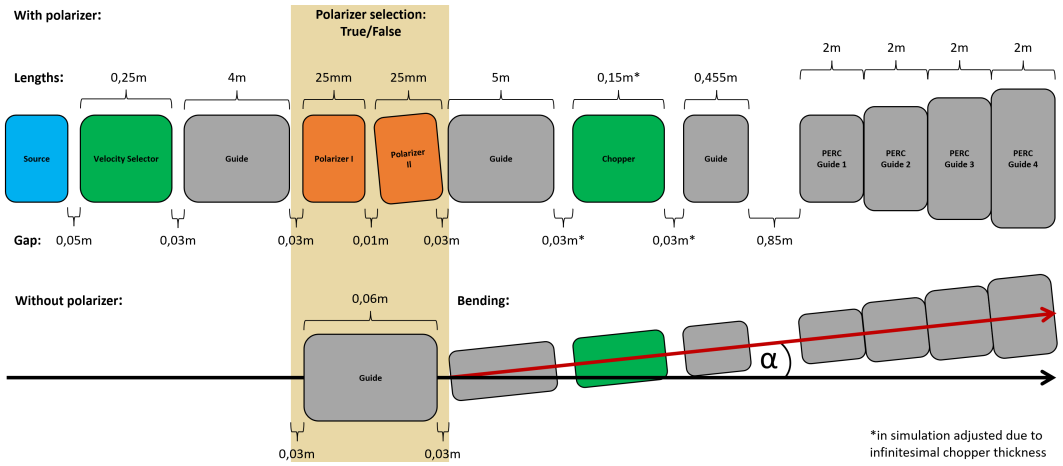

Figure 4.1: Visualization of the components used within the simulation template. Lengths of the components as well as gaps are given. Within the highlighted area one can choose whether a polarizer should be part of the setup or not. The beam axis can be adjusted by an angle α.

Since the cut-out is a special guide geometry, it could not be implemented with a single standard component. Hence the uncut part is realized by the mentioned "Guide_gravity"-component, which is then complemented by two rotated mirrors at the top and bottom. These mirrors have the same reflectivity parameters as the guides and enable therefore sufficient representation. Within the real setup, it might be necessary to shorten the first guide, due to the inhomogeneous magnetic field at the beginning. This shortening is foreseen within the template but currently set to zero. A sketch of the used setup is shown in figure 4.1.

Apart from the surroundings, to declare the instrument object and perform the simulation, the template is split into three main sections. Within the first section, variables are defined in a way that initializes them within the McStas code, but also enables Python analyses later on. The second section contains the setup of the experiment with the declaration of the components and the relative distances and rotations to each other. In a third section, the parameters are assigned to these components. An illustration is then given to allow a quick check.

A detailed unit test was performed for each used component. For instance wavelength spectra of the velocity selector, reflectivity parameters of the supermirrors and flux adaption of the chopper have been verified. In addition, cross-checks have been made with existing simulations by A. Hollering [28] and C. Klauser [34]. The resulting template is a Jupyter notebook named "PERC_Template.ipynb". It is continuously

updated and shared on GitLab. It is already being used for other purposes such as the polarizer selection.

In all upcoming simulations, 10^{10} neutrons are simulated. A check of the McStas simulations revealed that the statistical uncertainties are four orders of magnitude smaller than the values. Therefore, the statistical uncertainties are negligible and will not be listed or plotted. However, one has to keep in mind that the simulations include many uncertainties. The parameters might differ in the final setup, so they will need to be adapted within the template. The supermirrors for the neutron guides, for instance, have not yet been produced. Therefore, the used reflectivity parameters are only estimates evaluated from test samples. Figure A.2 shows a comparison of the neutron densities for three reflectivity curves with slopes that vary by 10 %. Additionally, although the waviness of the guides can be implemented, it is not defined within the upcoming simulations. Furthermore, alignment inaccuracies that will occur in the real setup are neglected. While distances can be measured quite accurately and many assumptions might be close to reality, the biggest uncertainty is the used source. No actual neutron spectrum at the beamsite could be measured yet, so the description of the could source can be off by 20 % or more [29]. Furthermore, the cold source at FRM II is currently not usable for operation. Therefore, absolute values for neutron flux and density will deviate, especially before the cold source is available. So although the following simulations do not include them, there are significant systematic uncertainties. Nonetheless, relative statements and optimizations are possible and estimates can be determined. The aim is to obtain an adequate model of the experiment and to gain an understanding of the effects that occur to provide an aid to decision-making.

Chapter 5

Neutron Density Optimization

The accuracy of experimental results is determined by systematic and statistical uncertainties. Systematic uncertainties can have many different causes, which have to be targeted specifically to minimize the uncertainty. For instance reducing detector gain drifts by temperature stabilization (of the detector and the readout electronics). Statistical errors, on the other hand, are mainly limited by the number of events N measured [35], as the relative statistical error is correlated with

$$\sigma_{\text{rel}} = \frac{N}{\sqrt{N}} = \sqrt{N}. \tag{5.1}$$

Therefore, to minimize the statistical uncertainty, one wants to increase the number of events the main detector of PERC detects to measure as many events as possible.

This can either be accomplished by measuring for a longer period of time, or by increasing the event rate. The detectors do not limit the measured event rate, as they can process higher rates. The limiting factor in PERC's case is the number of neutron decays occurring in the uniform magnetic field. Hence, one wants to increase this number by optimizing the neutron density within the decay volume, as the pulse length was already optimized in chapter 3.2.

5.1 Reduction Effects

Before discussing optimization opportunities, the three main effects that cause a reduced neutron density in PERC are explained.

5.1.1 Reflectivity

The neutrons are extracted from inside the reactor and need to be transported to the beam site, where the measurements can be performed. The transport is achieved by neutron guides, which use the principle of total external reflection. The guide system is evacuated, creating a vacuum. As mentioned in section 4.2, the incoming neutrons have a divergence of up to 1° after the velocity selector. Therefore, a neutron position

might change up to 17.4 mm in x- or y-direction per meter of flight in z-direction. The distance between velocity selector and beamstop is approximately 19 m to 20 m, which corresponds to up to 12 collisions with the guide, for a neutron of maximum divergence.

Total external reflection occurs when the wave encounters a material that has a Fermi potential higher than the energy E propagating perpendicular to the material surface. This is the case for angles up to a critical angle, that can be described by

$$\theta_{\mathrm{C}} = \arcsin\left(\sqrt{\frac{V}{E}}\right). \tag{5.2}$$

V is the material dependent Fermi potential, which is given by

$$V = \frac{2\pi\hbar^2}{m} nb. \tag{5.3}$$

Here, m is the mass of the neutron, $\hbar$ is the reduced Planck constant, b is the coherent scattering length and n is the number density [36]. A commonly used material is nickel as it has a high b as well as a high n and can be manufactured in very thin layers. For incoming neutrons with a wavelength of 5 Å, the angular acceptance of nickel is approximately 0.7° [20].

To achieve a higher angular acceptance, one can use so-called neutron supermirrors. Supermirrors are made of polished layers of varying thickness and alternating materials, which make use of diffraction. Using one material with a high neutron refractive index and one with a preferably negative neutron refractive index leads to a large difference at the connecting surface, making it more likely for neutrons to reflect. Unlike for total external reflection, losses occur when using diffraction. Hence, the reflection probability for angles above the critical angle is not 100 %. However, the reflectivity is significantly higher than for monolayers. This enables a more efficient neutron transport, resulting in a higher neutron density in the decay volume.

The m-value describes the factor that indicates how much larger the critical angle for a supermirror is compared to the critical angle for a single material layer, usually of nickel. It is defined by the angle, at which the reflectivity has dropped to 50 %. A typical reflectivity curve is shown in figure 5.1.

McStas describes the reflectivity with

$$R = \begin{cases} R_0, & \text{if } Q \leq Q_{\mathrm{C}} \\ \frac{1}{2}R_0\left(1 - \tanh\left[\frac{(Q - mQ_{\mathrm{C}})}{W}\right]\right) \cdot (1 - \alpha(Q - Q_{\mathrm{C}})), & \text{if } Q > Q_{\mathrm{C}}. \end{cases} \tag{5.4}$$

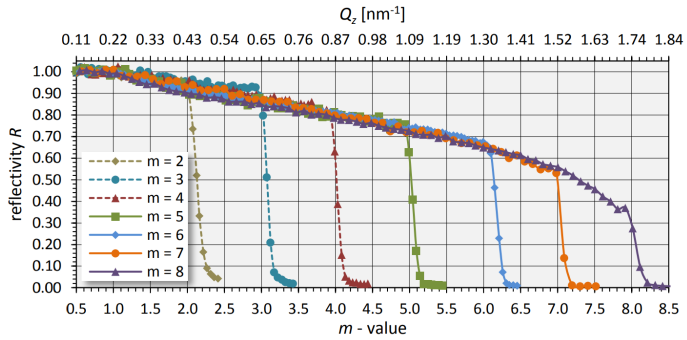

Figure 5.1: Reflectivity curves of Ni/Ti supermirror coatings with $2 \leq m \leq 8$. Here the definition of the m-value differs to the definition used in McStas and in this thesis. Image is taken from [37].

R_0 is the initial reflectivity (in case of total external reflectivity $R_0 = 1$), Q is the length of the scattering vector, and Q_C is the length of the scattering vector at the critical angle [38]. α describes the slope of the section where the reflectivity falls linearly and W describes the width of the drop-off at $Q = mQ_C$. Copper-titanium supermirrors, which were developed in-house, are to be used in PERC. The reflectivity of such a Cu/Ti supermirror has been measured, with neutrons of wavelength $\lambda = 5\,\text{Å}$, for different angles of incidence. The angle of incidence can be converted to a length of the scattering vector [39] with

$$Q = \frac{4\pi}{\lambda_n} \sin(\theta). \tag{5.5}$$

This enables the fit of function (5.4) to achieve an accurate description. The fit can be seen in figure 5.2, the resulting parameters are listed in table 5.1. Note that the low measured reflectivity for small angles is caused by the experimental setup, not by the actual reflectivity of the guide. As the m-value is defined by the critical angle θ_C, which depends on the materials properties, the same m-value results in different angles. To enable comparisons within this thesis, the m-value is given in dependence of the critical angle of nickel, if not mentioned otherwise.

Although the reflectivity is still 90 % at larger angles, losses in guide collisions cause the most significant reduction in neutron density. A neutron with a divergence of 0.75° in x- and y-direction, for example, reflects approximately 8 times between the velocity selector and the beamstop. With a reflection probability of $\approx 93.7\,\%$, that results in a survival probability of $0.937^8 = 59\,\%$.

The absorption also leads to a neutron density gradient inside the decay volume. Since this affects systematic effects, it is of interest to know the order of magnitude of

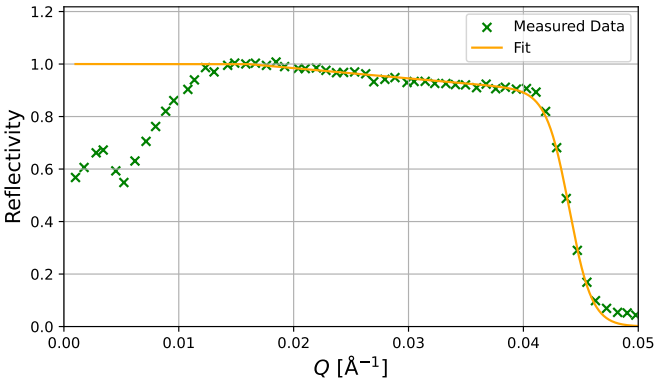

Figure 5.2: The reflectivity of a Cu/Ti supermirror as a function of the length of the scattering vector. The orange line is a fit of the function in equation (5.4), which McStas uses to describe the reflectivity. The low measured reflectivity for small angles is caused by the experimental setup and the non-zero reflectivity for larger angles might be caused by background.

Table 5.1: Results for the different fit parameters when fitting the reflectivity curve of the Cu/Ti supermirrors, which will be used for the guide in PERC.

Q_C	0.016
R_0	1
m	2.75 ± 0.01
α	3.87 ± 0.18
W	0.00198 ± 0.00005

the gradient. Therefore, a simulation considering only the reflectivity was performed. The simulation setup consists of the source, followed by the velocity selector, a 9 m long connection guide, and PERC's internal guide with a constant cross section of 60 mm × 60 mm. Every meter inside PERC, a detector is positioned that measures the neutron intensity over the whole cross section. As one can see in figure 5.3, the intensity drops by $\approx 7\,\%$ due to the interactions with the guide walls. This is comparable to the originally simulated 6 % reduction by C. Klauser [34].

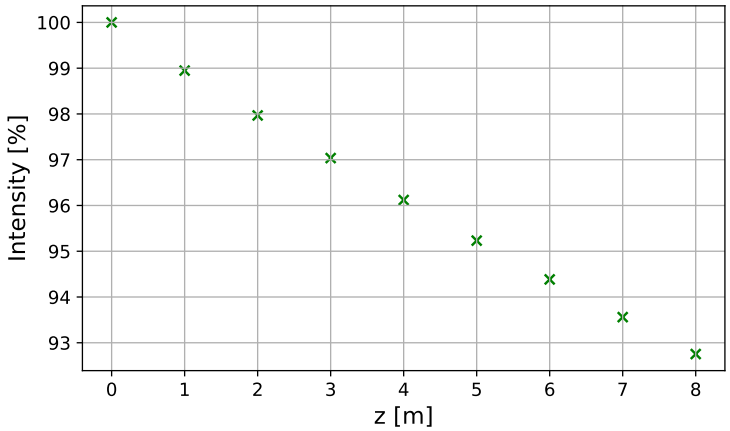

Figure 5.3: Simulated relative neutron intensity in PERC, over the length of the decay volume, only considering losses due to absorption in the guide.

5.1.2 Broadening

To perform proton asymmetry measurements in PERC, a ultra-high vacuum is needed. Creating the required ultra-high vacuum in an 8 m long guide with a cross section of 60 mm × 60 mm is impossible, due to the particle flow inside the guide at low pressures. In [33], a concept for the vacuum pump system of PERC is presented, with which it is possible to reach the required vacuum in the guide to perform proton asymmetry measurements. As mentioned in section 4.2, this concept includes pump slits every 2 m and a 2 mm broadening in width of the successive guides, increasing their cross section.

A larger cross section means fewer reflections, but also a reduced average density, as the same number of neutrons spreads out over more space. A visualization of that can be seen in figure 5.4. This needs to be considered, since only decays in the inner 50 mm × 50 mm are evaluated, to avoid edge effects. Hence, the number of measured neutron decays decreases by a factor of $\frac{A}{A+\Delta A} = \frac{60\times60\,\mathrm{mm}^2}{60\times66\,\mathrm{mm}^2} \approx 90.9\,\%$ by the end of the decay volume.

The simulation with the same setup as in section 5.1.1, but altered to include pump slits and broadening, and disregarding absorption losses, verifies this. A comparison of simulation and calculation can be seen in figure 5.5. Because it takes some distance for the beam to spread over the increased area, the intensity one meter after the broadening is higher than the calculated value.

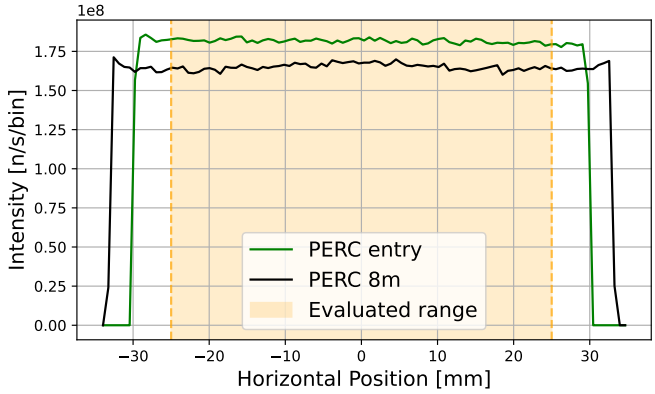

Figure 5.4: Horizontal cut of the neutron intensity at the beginning and end of the inner PERC guides. The guide width at the beginning is 60 mm, while at the end after 8 m it is 66 mm, when considering three pump slits. The highlighted range shows the area where neutron decays are analyzed. Although the integrated intensity remains constant, the integrated intensity for the evaluated area decreases, resulting in fewer measured neutron decays.

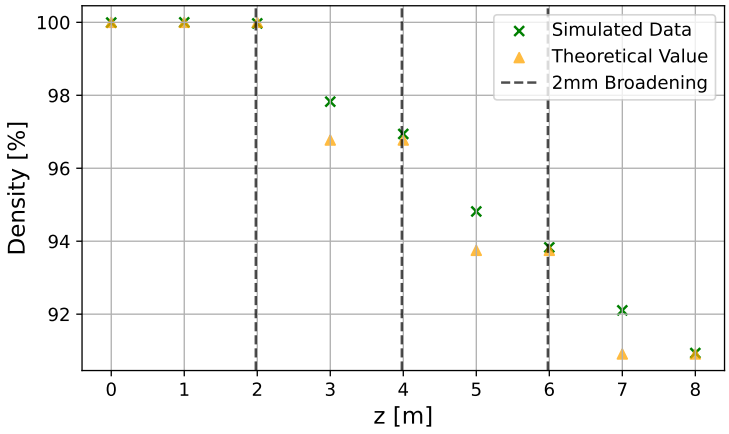

Figure 5.5: Average neutron density in the central 50 mm × 50 mm of PERC along the z-axis, normalized to the average neutron density at the beginning of the inner guide. The broadening of the guide every two meters is marked by black dotted lines. The simulation disregards absorption losses. The intensity one meter after the broadening is higher than the calculated value, as it takes some distance for the beam to spread. The simulated data fits the expected reduction as soon as the structure fades.

5.1.3 Gaps

Ideally, the neutron beam would be continuously contained in a guide, without gaps out of which neutrons can escape. However, screws need to be accessible and guides cannot be mounted on rotating or vibrating components, like the velocity selector or the chopper. At these components, there are gaps in the guide, out of which the neutrons can escape, reducing the neutron density. In PERC, there has to be an additional significant gap in the guide so that the electrons are able to reach the backscatter detectors (see figure 4.1).

At each gap, neutrons that would normally reflect of the guide are lost, since they are not coupled into the next guide after the gap. The loss probability correlates with the length of the gap. Neutrons with a large divergence are more affected, since they rely more on the confinement by the guide. This can be seen in figure 5.6. Therefore, gaps have a slight focusing effect at the expense of neutron density.

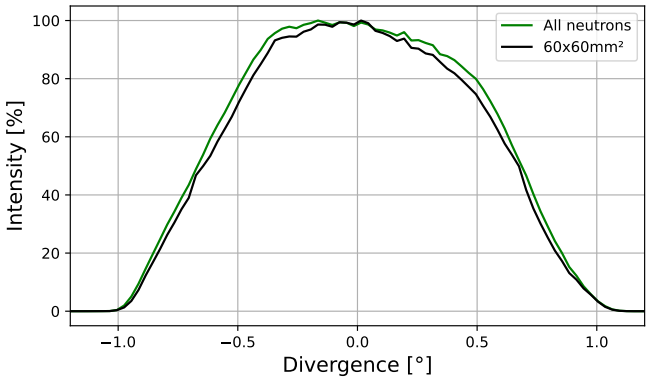

Figure 5.6: One dimensional divergence distribution of neutrons at the entry of the inner guide, after a gap of 85 cm. The green curve considers all neutrons at that position, while the black considers only the neutrons in the central 60 mm × 60 mm, which are able to enter the guide. Each distribution is normalized to the highest value. One can see a slight focusing effect due to the gap.

Not only is the divergence affected, but also the spatial distribution, which had been uniform before the gap. While the neutrons traveling towards the center of the beam are unaffected, the lack of reflections at the edges causes a decrease in intensity, resulting in a slope. The previously sharp rectangular distribution softens. This effect is visualized in figures 5.7 and 5.8. The plots show, what the neutron density distribution looks like 1 m and 2 m after the gap. Even after 2 m there is still a noticeable structure. In the described experimental setup, the structure takes

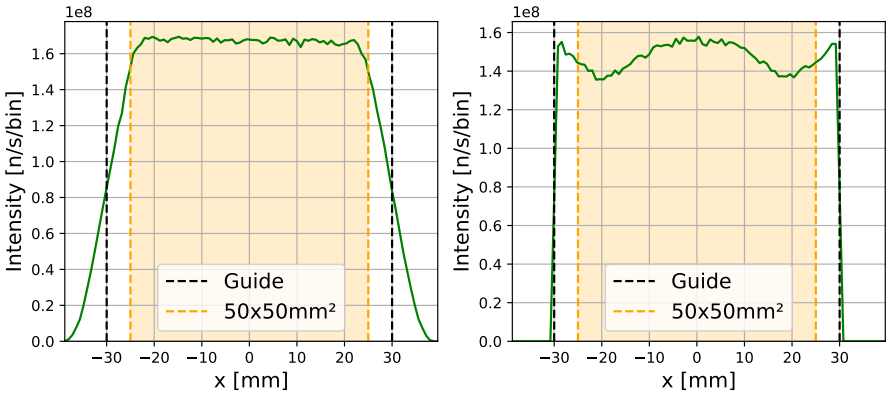

Figure 5.7: The neutron intensity distribution along the x-axis after a 0.5 m long gap (left) and the neutron intensity distribution inside the guide 1 m after the gap (right). The black lines show where the guides borders are, while the orange lines and shading indicate the area of interest. Part of the neutrons can not couple into the following guide. The slopes cause a non-uniform distribution.

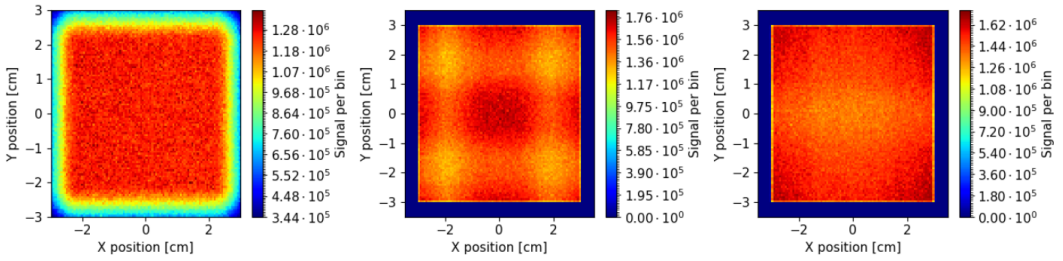

Figure 5.8: Neutron intensity as a heatmap over the beam cross section at 0 m, 1 m and 2 m after a 0.5 m gap. One can see the structure caused by the gap. Since the pattern develops in both directions, the gradient is even bigger in areas of overlap.

approximately 4 m to wash out and return to a rectangular neutron distribution.

To summarize, gaps have two effects that influence the average neutron density in the inner 50 mm × 50 mm. First the loss of neutrons. Secondly, the pattern in the distribution. Therefore, large gaps in particular massively shape the beam profile and must be considered, when evaluating the neutron density inside the measured area.

5.1.4 Combination

Within PERC all three effects combined form the effective neutron density gradient. To analyze the effects, a simulation with reasonable gaps, broadening, and the reflectivity parameters mentioned in table 5.1 was performed. Polarizer and chopper were excluded. A gap of 85 cm was implemented between the intermediate guide and the PERC guides, to give the electrons sufficient space to reach the backscatter detector.

The results of the simulation are shown in figure 5.9. The green markers show the intensity over the whole area, which essentially disregards the broadening effect. In comparison to figure 5.3, one sees a slightly lower neutron loss, which can be explained by the broadening of the guides, resulting in fewer reflections and hence a

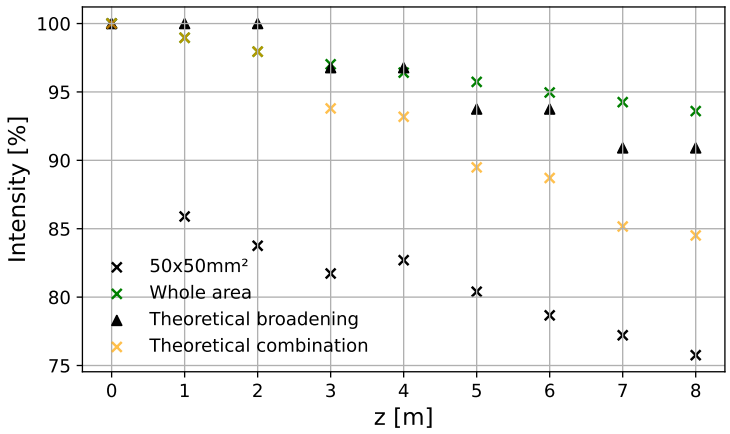

Figure 5.9: Relative decrease in neutron intensity in PERC split up in different effects. Values are normalized to input value. The black markers show the relative intensity in the central 50 mm × 50 mm. The green markers show the relative intensity over the whole cross section, which shows reflectivity losses. The black triangles are the theoretical expectation due to the broadening. The orange markers combine theoretical broadening and reflectivity losses.

higher survival probability. The black triangles show the expected reduction of intensity in the central 50 mm × 50 mm due to broadening. Considering the theoretical broadening for the green data results in the orange data. The black markers show the intensity in the inner 50 mm × 50 mm, combining all effects. Here, the intensity at 0 m is increased due to the incoming beam profile, which shifts the normalization. If one were to normalize, using the intensity over the whole cross section with a factor of $\frac{50\times50\,\mathrm{mm}^2}{60\times60\,\mathrm{mm}^2}$, the orange and black markers would converge towards the end of the decay volume, when the gap structure washes out.

5.2 Optimizations

Since the cold neutron source at the FRM II is currently out of operation, the intensity of the neutrons at the wavelength of interest is reduced by a factor of ten or more. As a result, maximizing the neutron intensity inside the uniform decay volume is of special interest, in order to reach reasonable statistics. In the following sections possible optimizations are analyzed and critically discussed.

Here the simulations use a simplified template compared to the one described in section 4.2. They use the source file describing the neutron distribution after the MEPHISTO guide. This is followed by the velocity selector and a 9.051 m long guide, from now on called "connection guide". Then one 6 cm gap to represent the part where usually chopper and a gap on each side would be. The chopper is not part of the setup. It follows the additional guide of 45.5 cm length, from now on called "intermediate guide". The intermediate guide is followed by an 85 cm long gap, leading to the internal guides of PERC, which remain unchanged. A sketch is shown in figure 5.10. Each run is done simulating a total of 10^{10} neutrons. The statistical errorbars are therefore negligibly small and are not included in the plots. As previously mentioned the accuracy is systematically limited, especially by the source description.

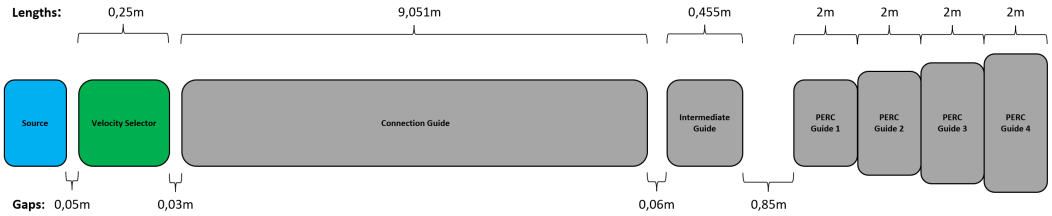

Figure 5.10: Sketch of the simplified setup of the beamline for optimization simulations.

Table 5.2: Comparison of parameters for selected wavelengths 5 Å and 4.5 Å. Although the measured time period and frequency changes, the measurement time per second is identical.

	5 Å	4.5 Å
f_{rot}	48.7 Hz	54.0 Hz
t_{signal}	2.92 ms	2.63 ms
$t_{\text{background}}$	1.69 ms	1.52 ms
$t_{\text{meas,s}}$	142 $\frac{\text{ms}}{\text{s}}$	142 $\frac{\text{ms}}{\text{s}}$

5.2.1 Wavelength

In equation (3.6) the velocity-wavelength correlation is described. Neutrons with a lower wavelength are faster. Figure 3.4 shows that the next pulse can begin as soon as the reflected neutrons of the previous pulse have reached the guide and the background has been measured. Faster neutrons need less time to cross this distance, resulting in a higher possible repetition rate. However, the time period for decay measurements also depends on the velocity of the neutrons, as they spend less time in the uniform magnetic field. The gain in measured events due to a higher repetition rate cancels out with the loss due to a shorter measurement period, as one can see in table 5.2, where $t_{meas,s}$ is the measurement time per second. As a result, it usually has no statistical advantages to use neutrons with lower wavelengths. Material considerations as discussed in chapter 3 favor slower neutrons instead.

In our case, there is an additional factor to be considered, which is the wavelength spectrum after the MEPHISTO guide, shown in figure 5.11. One can see, that the neutron intensity is considerably higher for lower wavelengths, which makes the usage of shorter wavelengths interesting. Furthermore, the divergence is slightly lower for faster neutrons.

The velocity selector is limited to a rotation frequency of 472 Hz, which allows the use of wavelengths as short as 4.5 Å [31]. A simulation was performed to compare the neutron density in PERC for a wavelength of 4.5 Å and the originally planned 5 Å. The neutron densities, as well as the relative gain are plotted in figure 5.12. As one can see, using a wavelength of 4.5 Å instead of 5 Å, leads to an average gain of 9 % within the uniform magnetic field from 1 m to 7 m. The adaption places approximately 10 % higher demands on the chopper's rotational frequency and therefore leads to higher loads, but this is still within reasonable limits. The geometry of the chopper, as well as the opening function (see section 3.3), remain the same, as the relative timings, which determine the layout, do not change.

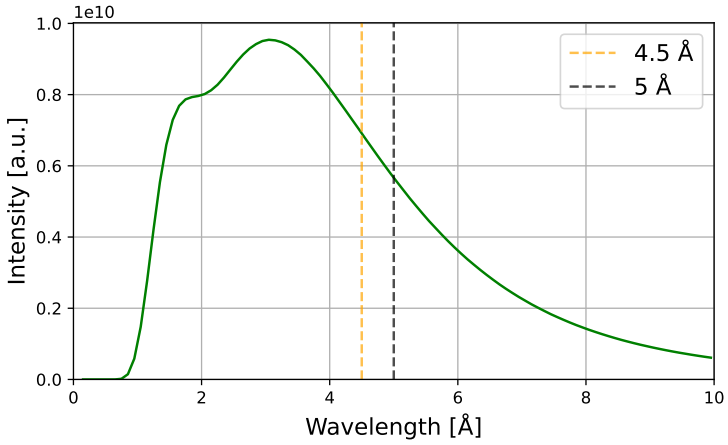

Figure 5.11: Wavelength spectrum after the MEPHISTO guide, going into the velocity selector. The two wavelengths considered in the optimization are highlighted. Compared to 5 Å, the intensity increases, when moving to shorter wavelengths up to ≈ 3 Å.

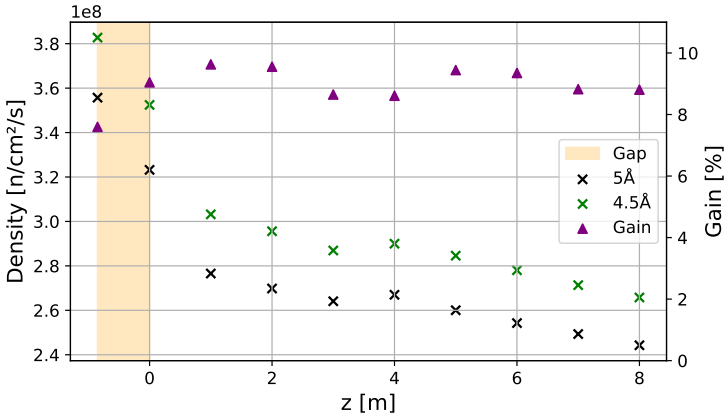

Figure 5.12: Average neutron density after the intermediate guide up to the end of PERC for 5 Å (black) and 4.5 Å (green). The beginning of PERC is located at $z = 0$ m. The gain is shown in purple. The setup with a shorter wavelength shows a higher average density.

It is currently being checked, if a wavelength of $\lambda = 3\,\text{Å}$ can be selected with a reasonable transmission, by tilting the velocity selector. Figure 5.11 shows that at 3 Å compared to 5 Å the neutron intensity is by a factor of $\frac{0.95}{0.55} \approx 1.7$ higher. However, the neutrons are significantly faster, which results in a much higher chopper frequency as one can see in table 3.1. Therefore, similarly to section 3.6, a two-window chopper disc might become necessary for neutrons with an average wavelength of $\lambda = 3\,\text{Å}$.

5.2.2 Increased Height of Connection Guides

Currently, the connecting guides from the velocity selector, up to the entry of PERC are planned with a cross section of 60 mm × 60 mm. The MEPHISTO guide also has a width of 60 mm, but a height of 106 mm. The switch in cross section in the setup is chosen to take place after the velocity selector. Due to the gap effect, the intensity profile when entering PERC is not uniform, as one can see in figure 5.7. The idea is to choose connecting guides, that are high enough, so that the slope on the edges does not reach the inner 60 mm that couple into the PERC guides. This essentially means that additional neutrons couple into the connection guide and are absorbed at a later point. As a result, one still cuts off part of the neutrons coming from the connection guide, but the adaption inside PERC does not occur, since the profile entering is already uniform.

This should halve the gap effect as one of the two directions is dealt with. With a maximum divergence of approximately $\theta \approx 1°$ for an $m = 2$ guide, which translates to a displacement $\Delta x_{\text{max}} = \Delta y_{\text{max}} \approx 17.4\,\frac{\text{mm}}{\text{m}}$ and a gap of 85 cm, the gain is expected to saturate with a cross section of 60 mm × 90 mm. This is the height needed, so that the edges are located outside the cross section, that is entering the PERC guides. In figure 5.13 the simulation results for different heights of the connecting guides are shown. The assumption is verified and one can see that the gain does saturate at approximately 90 mm. However, it is advised to use connecting guides with a height of 80 mm, as the gain is almost identical to the gain with 90 mm height, while less absorbing material is needed. Within the uniform magnetic field, the gain when using such a guide is around 13 % compared to a guide with 60 mm height.

However, this optimization has the disadvantage, that more excess neutrons need to be absorbed at the beginning of the PERC guides, which increases the background and requires more shielding. This additional material may also affect the achievable vacuum. Nonetheless, no additional components are needed, since it was already foreseen to place a neutron absorber there for shielding.

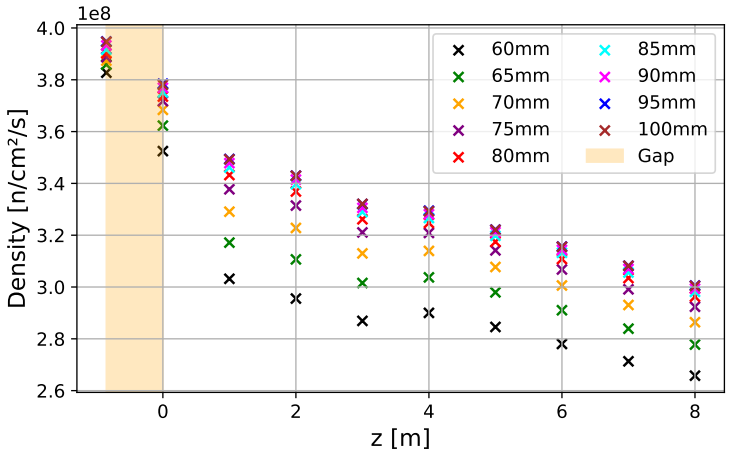

Figure 5.13: Average neutron density inside PERC for varying heights of connecting guides between velocity selector and PERC. The beginning of PERC is located at $z = 0\,\mathrm{m}$. The average neutron density increases by using a higher connection guide. When the coupling part of the neutron beam is uniform, the effect saturates.

5.2.3 Increased Height of PERC Guides

Increasing the height of the connection guide to 80 mm does not yet fully utilize the height of the MEPHISTO guide. It was established, that increasing connection and intermediate guide further shows no significant gain. Nonetheless, heightening all guides is an option. The dimensions of the guides in PERC are, however, limited and can only go to a height of 70 mm. This increases the size of the connecting guides to $60\,\mathrm{mm} \times 90\,\mathrm{mm}$, as one has to add the extra 20 mm. A height of 90 mm is still within the height of the MEPHISTO guide. A slight additional advantage is the decrease in the number of reflections due to the greater height. As the gain is predominantly geometric, it is expected that, apart from the aforementioned advantage, the average density remains the same while the total intensity increases due to the larger usable area. With the outer 5 mm not being used due to edge effects, that would increase the analyzing area from $50\,\mathrm{mm} \times 50\,\mathrm{mm}$ to $50\,\mathrm{mm} \times 60\,\mathrm{mm}$, so a 20 % gain is expected.

Figures 5.14 and 5.15 show the results of simulations, comparing the setups. As expected, the average density is similar in both setups, while the absolute intensity is increased for the higher guide. The gain is 21 % within the uniform decay volume, thus an increased height should be considered. Increasing the height places many demands on other components, for example the detectors must be large enough to cover the increased area. Furthermore, it needs to be ensured that the electrons and protons can pass the magnetic filter over the whole area and the beamstop must be

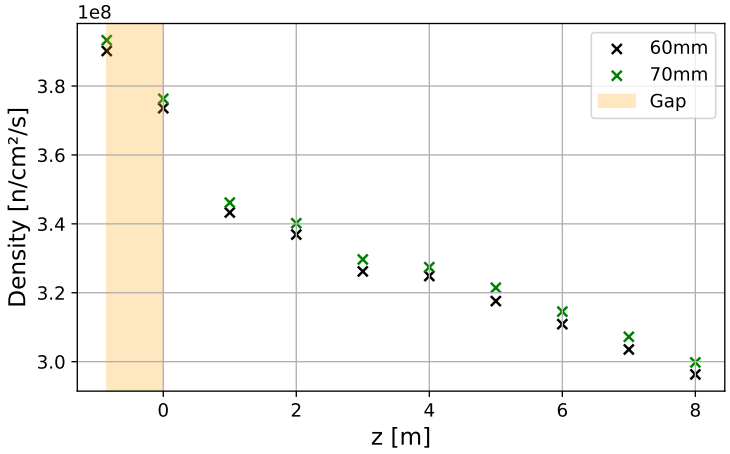

Figure 5.14: Average neutron density in PERC for 60 mm and 70 mm height of the internal PERC guides. The beginning of PERC is located at $z = 0$ m. The connection guide is 20 mm higher than the internal guides. As expected, both densities are almost equal, with the slight difference being caused by the decrease in reflections within a higher guide.

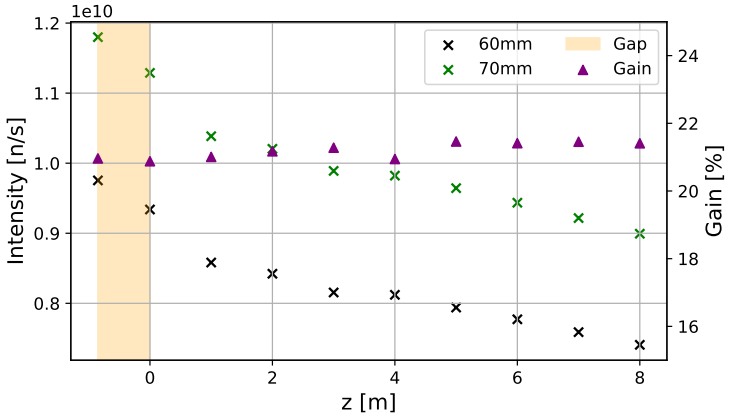

Figure 5.15: Absolute neutron intensity in PERC for different heights of the internal PERC guides. The beginning of PERC is located at $z = 0$ m. The connection guide is 20 mm higher than the internal guides. The gain is shown in purple. With an increase in height, the evaluated area increases from $50 \times 50\,\text{mm}^2$ to $50 \times 60\,\text{mm}^2$ (outer 5 mm disregarded due to edge effects), resulting in more measurable neutron decays.

increased in size and so on. The feasibility of increasing the height is currently being studied. If verified, increasing the height is a very good option to increase statistics.

5.2.4 Increased Width of PERC Guides

Increasing the width of the PERC guides is not as lucrative, since the MEPHISTO guide is only 60 mm wide. There are no excess neutrons in that dimension that could be utilized. Each increase in width therefore comes with a decrease in density. However, there is the option of increasing only the width of the guides inside PERC. For the width, the spatial constraints are less limiting (than for the height) and a width around 80 mm should be possible. Such an increase prevents the loss of neutrons at the gaps before the decay volume. Furthermore, the severity of the discarded outer 5 mm lessens, as the ratio between considered and discarded decays increases. The losses due to the gap are expected to disappear completely when broadening the guides in PERC to 90 mm. Instead of only considering the uniform region, all neutrons should couple into the guide.

In figure 5.16 the results of the simulations with different widths are plotted. As expected, the average density decreases, as the neutrons distribute over a larger area. However, the increase in usable area makes up for the decrease in density, as can be seen in figure 5.17. With an increase to 70 mm (similar to section 5.2.3) the gain is 11 %. With a width of 80 mm, the gain is 17 %. Nevertheless, this optimization is less lucrative than the increase in height. Even if the increase in width is found

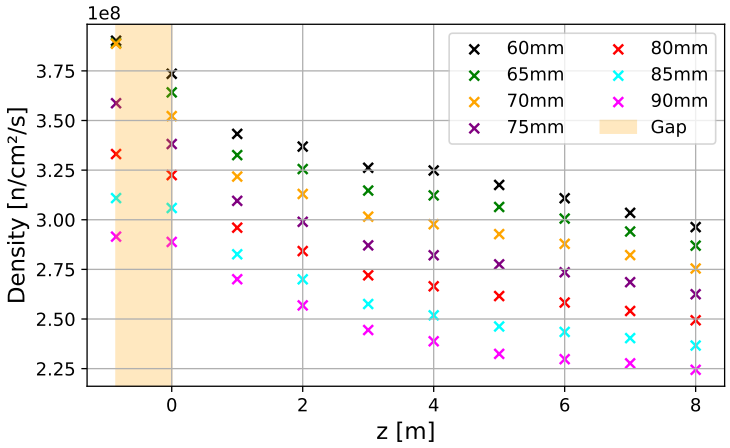

Figure 5.16: Average neutron density for different widths of the internal PERC guides. The beginning of PERC is located at $z = 0$ m. The average density decreases, as the neutrons, coming from the connection guide, spread over an increased cross section.

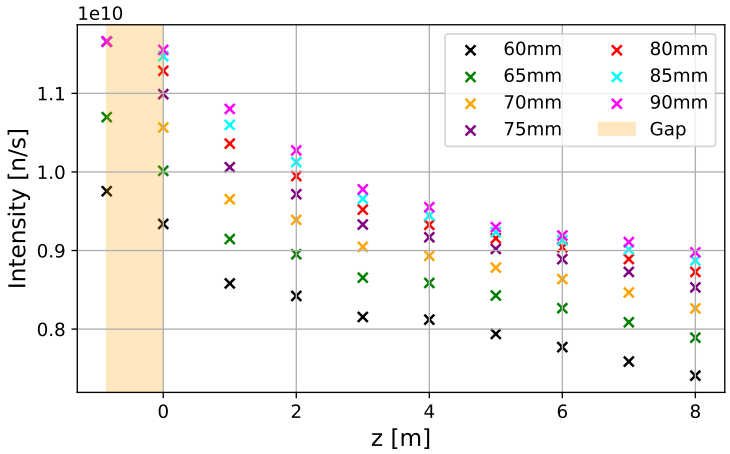

Figure 5.17: Neutron intensity for different widths of PERC guides. The beginning of PERC is located at $z = 0\,\mathrm{m}$. Although the average density decreases (see figure 5.16), the measured area increases, resulting in a higher intensity.

to be technically feasible, the gain is a lot smaller. It should also be noted that the structure within the guide is much more pronounced, as the entire profile shown in figure 5.7, including the slopes, couples into the PERC guides. Due to the wider guides, the structure also takes longer to fade, meaning that a gradient in neutron density is present over the whole decay volume. Hence, a higher setup should be prioritized over a broader one.

5.2.5 Widening of Connection Guides

A broadening of the entire connecting guides would not lead to a significant gain, because the width of the MEPHISTO guide is fixed. The coupling profile would be made uniform, but then the reduction in intensity would be greater than in the gap effect, as less neutrons couple into the inner guides. As result, one reduces the density, shifts the position of absorption and adds the disadvantages mentioned in section 5.2.2.

However, a widening of the connection guide might be favourable. With the previous optimization the cross section of the connecting guide is $60\,\mathrm{mm} \times 80\,\mathrm{mm}$. This could be linearly widened to $70\,\mathrm{mm} \times 80\,\mathrm{mm}$ at the exit. Reflections along a guide with increasing cross section, decrease the angular divergence, as the angle of incidence is lower. This has a focusing effect on the beam, resulting in a lower neutron loss at the gap. However, the average neutron density decreases, since the cross section increases. To check the overall effect of a widened connection guide on the neutron

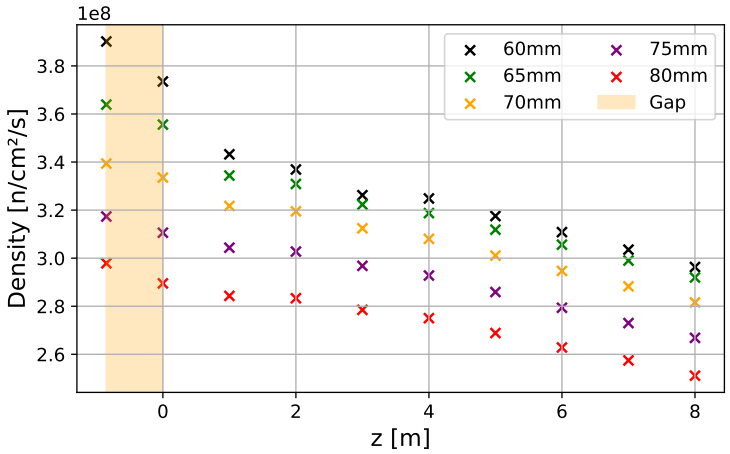

Figure 5.18: Average neutron density in PERC for varying widening of the connection guide between velocity selector and PERC. The width at the entry of the connection guide is 60 mm. The width at the end is labeled in the legend. The beginning of PERC is located at $z = 0$ m. Although the gap losses decrease, no widening results in an increased average density in PERC.

intensity, simulations were performed. The intermediate guide was adapted to have a constant cross section of the same size as the end of the connection guide. The results of the simulations can be seen in figure 5.18. Unfortunately, the density reduction due to the increased area is too significant and a widening of the connection guide does not result in a higher neutron density.

5.2.6 Widening of all Guides

The problem with the linear increase in the cross section of the connection guide is the reduced intensity. As discussed in section 5.2.4, it is also possible to increase the width of the guides in PERC. Adjusting all guides might be of interest. Compared to only broadened guides in PERC, this is expected to have a lower average density in PERC due to gap losses. However, linearly increasing the width of the connection guide results in a fading of the structure before the inner guides, while also reducing the angular divergence of the neutrons. Therefore, it is still interesting to take a look at this setup. Hence, simulations with a linear widening of the connection guide and a constant increased width of the intermediate- and PERC guides are done.

The average densities and intensities for the different setups are shown in figures 5.19 and 5.20. The advantages and disadvantages are the same as in section 5.2.4. Figure 5.21 shows the neutron intensity when widening the connection guide and broadening

the PERC guides to 80 mm. A comparison to only broadening the PERC guides to 80 mm is included. At the beginning of PERC the intensity when widening both guides is approximately 10 % lower, but the intensities converge to nearly the same value at the end of the decay volume. On average, the difference is only 2 %. As the widening of all the guides leads to a higher beam uniformity, which is beneficial for systematics, and a comparable intensity, this should be considered, if broader guides are chosen for inside PERC.

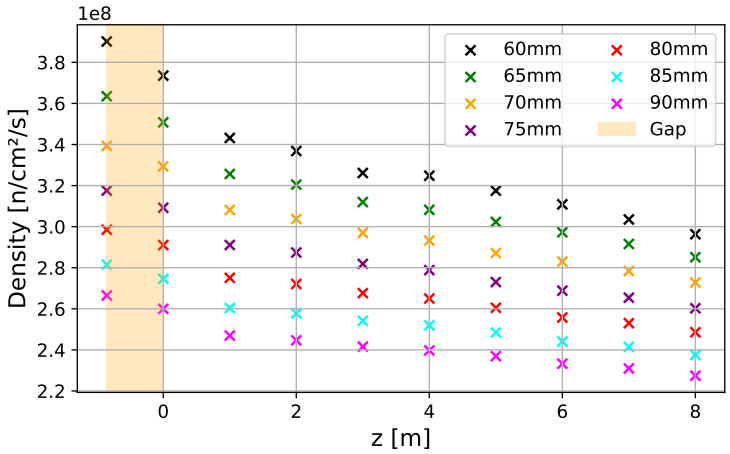

Figure 5.19: Average neutron density in PERC for varying widening of the connection guide between velocity selector and PERC. The width at the entry of the connection guide is 60 mm. The guides in PERC have the same cross section as the end of the connection guide (labeled in the legend). The beginning of PERC is located at $z = 0$ m. The average density decreases, as the same number of neutrons spread over an increased cross section.

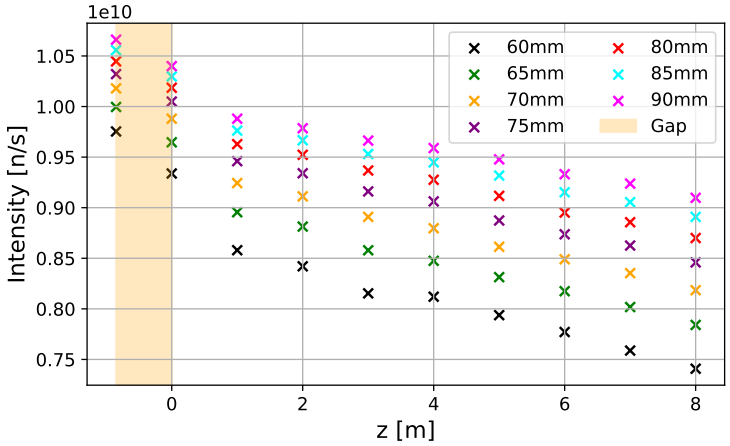

Figure 5.20: Neutron intensity in PERC for varying widening of the connection guide between velocity selector and PERC. The width at the entry of the connection guide is 60 mm. The guides in PERC have the same cross section as the end of the connection guide. The beginning of PERC is located at $z = 0$ m. The analyzed width is 10 mm smaller than the given width to avoid edge effects (5 mm per side). The increased cross section is more significant than the reduction in density, leading to a higher intensity.

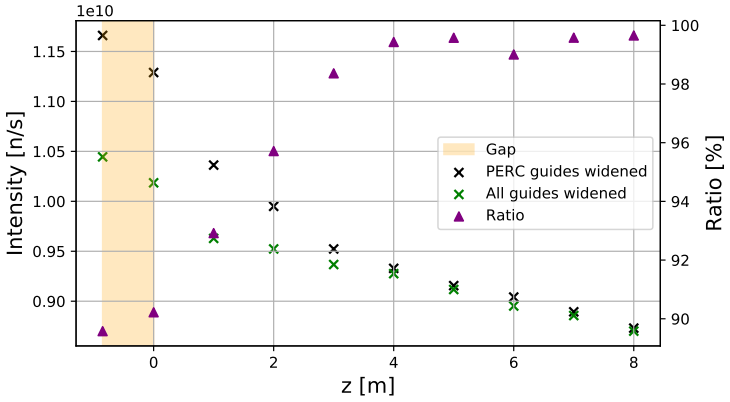

Figure 5.21: Comparison of neutron intensities for broadening of PERC guides on its own and the combination of the widened connection guide and broadened PERC guides. In both setups, the increased width is 80 mm. The beginning of PERC is located at $z = 0$ m. The increased cross section of the connection guide leads to a lower coupling intensity, but both intensities converge inside the decay volume.

5.2.7 Narrowing of Connecting Guide

Up to now, only the effects of broader and higher guides on the neutron intensity have been analyzed. However, there is also an argument to be made for narrowing the connection guide between velocity selector and the entry to PERC. One could decrease the width of the connecting guide linearly, in order to force neutrons that would normally be lost at the gap to reflect in the last part of the connection guide before exiting it. This aims to minimize losses due to neutrons not coupling into the following guide. However, there is a trade-off, between low angular divergence and high neutron density. By using this configuration, the angle of incidence is increased, so using supermirrors with the same m-value for this guide would lead to more absorption. To reduce this, the simulation is run with a connection guide made of $m = 3$ supermirrors, increasing the critical angle. However, the absorption slightly increases, due to the lower reflectivity at higher angles.

Building on the results of section 5.2.2, the narrowing is only considered for the width of the connecting guides, with the intermediate guide having the same width as the end of the connection guide. The results of these simulations are shown in figure 5.22. One obtains an increased average neutron density after the intermediate guide and for the first two meters inside PERC. Due to the higher angular divergence, the density decreases quickly to a value similar to the setup without narrowing. Since

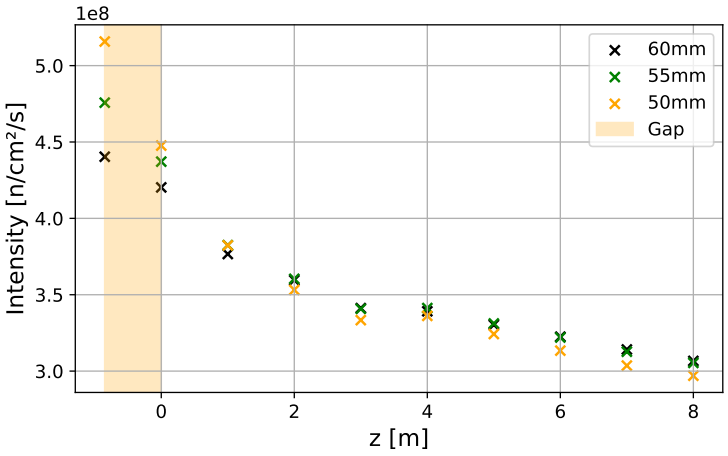

Figure 5.22: Average neutron density for varying narrowing of the connection guide between velocity selector and PERC. The width at the entry of the connection guide is 60 mm. The beginning of PERC is located at $z = 0$ m. While the average density is increased when coupling in, it quickly decreases inside the decay volume, resulting in no significant gain.

Table 5.3: Reflectivity parameters for the Cu/Ti supermirror and a commercially available non-depolarizing Ni/Ti supermirror for the implementation in McStas. The m-value 2.75 of Cu/Ti supermirrors in McStas corresponds to $m = 2$. Although the use of $m = 2.5$ would be sufficient, $m = 3$ is simulated for the Ni/Ti supermirrors because the corresponding reflectivity curve is available [37].

	Cu/Ti	Ni/Ti
m	2.75	3
R_0	1	1
Q_C	$0.016\,\text{Å}^{-1}$	$0.022\,\text{Å}^{-1}$
α	3.876	4.487

the uniform magnetic field of PERC is approximately from 1 m to 7 m, the effective gain is very small and not worth the effort of implementing such a construction.

5.2.8 Guide Type

The MEPHISTO guide have an m-value of 2.5 while the copper-titanium guides that are planned for PERC have an m-value of 2. This means that the critical angle within MEPHISTO guide is higher. It is currently planned to use copper-titanium guides from the velocity selector onward. Therefore, the neutrons of high angular divergence are absorbed within the connection guide, which reduces the density gradient in PERC. However, if the target is to maximize the neutron density, one has to consider using a different type of supermirror for the guide, that can transport all neutrons exiting the MEPHISTO guide. For example, a commercially available non-magnetic nickel-(molybdenum)-titanium neutron guide from SwissNeutronics with an m-value greater than 2 could be used [40].

Simulations comparing the different guide types were performed, the results of which are shown in figure 5.23. The initial density, going into the connection guide, is identical, but the different guide types result in different densities at the end of the connection guide. Since the MEPHISTO guide uses $m = 2.5$ any value higher than that for the connection guide does not result in a higher density as the neutrons with higher divergence are already lost. A detailed comparison of the Ni/Ti guide with $m = 3$ and the Cu/Ti guide can be seen in figure 5.24, the parameters of the compared guides are given in table 5.3, their reflectivity curves are shown in figure A.3. Throughout the whole setup, the neutron density is higher when a guide with higher m is used, even though the additional neutrons have a higher divergence and are therefore more likely to be lost at the gap. Using an $m = 3$ Ni/Ti guide instead of the $m = 2$ Cu/Ti guide one gains an average of 5 % in the range from $z = 1$ m to $z = 7$ m. This is a significant gain, but it comes with an increase of background, because

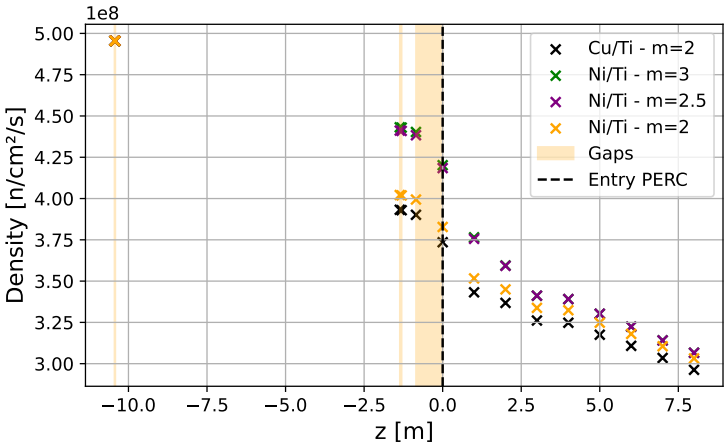

Figure 5.23: Comparison of the average neutron density from velocity selector onward for guides made out of different types of supermirrors. The beginning of PERC is located at $z = 0\,\mathrm{m}$. Using Ni/Ti supermirrors results in a higher density, with a saturation at $m = 2.5$.

the neutrons with larger angles are absorbed by the PERC guides. Furthermore, it causes a higher gradient in the density within the decay volume. From $z = 1\,\mathrm{m}$ to $z = 7\,\mathrm{m}$, the neutron density decreases by 12 % when using copper-titanium guides, but by 17 % when using $m = 3$ nickel-titanium guides. Hence, one has to decide if a 5 % gain is worth increased background and the systematic effects of the larger gradient.

5.2.9 No Broadening within PERC

As explained in section 4.2, guides within PERC are planned to be 2 mm broader after every pump gap, which leads to a reduced intensity but has the advantage that no neutrons are lost at the gaps. However, one could also keep the width of the guides constant. This would cause some neutron losses but has the advantage that the cross section stays constant. Therefore, guides of constant width might be favorable. The results of simulations comparing the two setups are plotted in figure 5.25. Since the first pump gap is located at two meters, this is where the setups start to show differences. At the end of the uniform magnetic field at $z = 7\,\mathrm{m}$, the density is 7 % higher without broadening than with broadening. The average gain is 3 %. The setup without broadening also decreases the density gradient within PERC. From $z = 1\,\mathrm{m}$ to $z = 7\,\mathrm{m}$, the neutron density decreases by 5 % when the cross section is constant, but by 12 % when broadening after every gap. However,

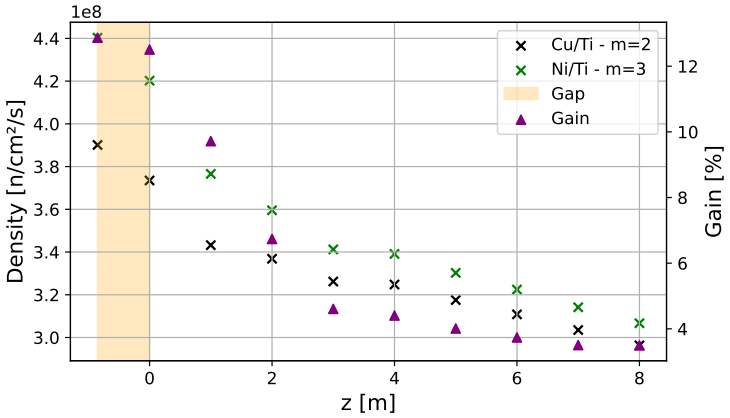

Figure 5.24: Average neutron density for different guide types. The beginning of PERC is located at $z = 0\,\mathrm{m}$. The gain is shown in purple. Using Ni/Ti supermirrors results in a higher density, but also a steeper density gradient.

one would need to place shielding material around each gap to absorb the neutrons that are lost.

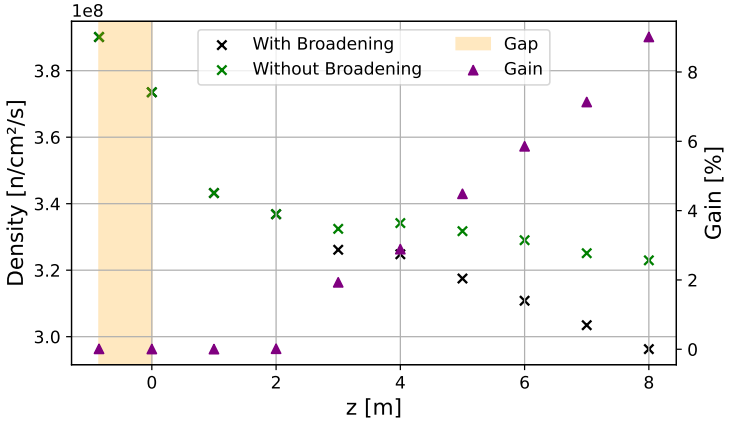

Figure 5.25: Average neutron density with (black) and without broadening (green) of the guides after each pump gap within PERC. The beginning of PERC is located at $z = 0\,\mathrm{m}$. The gain is shown in purple. The setup with a constant cross section has a higher average neutron density, as well as a lower density gradient within the decay volume.

5.2.10 Summary

Several ways to increase the neutron intensity were identified. The feasibility of some changes has to be checked, especially the increase in width and height of the guides in PERC. The event rate increases by nearly 90 %, when selecting a wavelength of 4.5 Å, an $m = 2.5$ non-depolarizing Ni/Ti with a constant height of 70 mm and a constant width of 80 mm for the inner guide, and a connection guide with a constant height of 90 mm. This increase is with respect to the standard geometry described in section 4.2. Furthermore, there is a systematic uncertainty, as the simulation setup is idealized and the accuracy of the source description has to be verified with measurements. Nonetheless, such an increase of the event rate reduces the measurement time by almost a factor of 2. Table 5.4 shows all of the optimization parameters and the resulting gain.

Table 5.4: Intensity and gain of the different optimization possibilities. The intensity is averaged over the volume with uniform magnetic field from $z = 1$ m to $z = 7$ m. The outer 5 mm are discarded to avoid edge effects. The first row of each section shows the value for an unaltered setup against which the following rows are compared. As 10^{10} neutrons are simulated, the statistical uncertainties are negligible.

Optimized parameter	**Intensity in analyzed area [n/s]**	**Gain [%]**
Adapted wavelength		
5 Å	6.57×10^9	0
4.5 Å	7.18×10^9	9.3
For all simulations below, a wavelength of 4.5 Å was used. Apart from that and the optimized parameter in the first column, the standard geometry of section 4.2 applies.		
Increased height of the connection guide		
60 mm × 60 mm	7.18×10^9	0
60 mm × 65 mm	7.52×10^9	4.7
60 mm × 70 mm	7.79×10^9	8.5
60 mm × 75 mm	7.97×10^9	11.0
60 mm × 80 mm	8.08×10^9	12.5
60 mm × 85 mm	8.14×10^9	13.4
60 mm × 90 mm	8.18×10^9	13.9
60 mm × 95 mm	8.21×10^9	14.3
60 mm × 100 mm	8.21×10^9	14.3

Optimized parameter	**Intensity in analyzed area [n/s]**	**Gain [%]**
For all simulations below, a wavelength of 4.5 Å and a connection guide height of 80 mm were used. Apart from that and the optimized parameter in the first column, the standard geometry of section 4.2 applies.		
Increased height of the PERC guides		
60 mm × 60 mm	8.08×10^9	0
60 mm × 65 mm	8.94×10^9	10.6
60 mm × 70 mm	9.80×10^9	21.3
Increased width of the PERC guides		
60 mm × 60 mm	8.08×10^9	0
65 mm × 60 mm	8.59×10^9	6.3
70 mm × 60 mm	8.99×10^9	11.3
75 mm × 60 mm	9.27×10^9	14.7
80 mm × 60 mm	9.46×10^9	17.1
85 mm × 60 mm	9.60×10^9	18.8
90 mm × 60 mm	9.71×10^9	20.2
Widening of the connection guide		
(60 → 60 mm) × 80 mm	8.08×10^9	0
(60 → 65 mm) × 80 mm	7.94×10^9	−1.7
(60 → 70 mm) × 80 mm	7.66×10^9	−5.2
(60 → 75 mm) × 80 mm	7.27×10^9	−10.0
(60 → 80 mm) × 80 mm	6.82×10^9	−15.6
Widening of the connection guides and broadening of the PERC guides		
The optimized parameter below shows the width. The connection guides are widened from (60 → xx mm) × 80 mm. The PERC guides have a constant cross section of xx mm × 60 mm.		
60 mm	8.08×10^9	0
65 mm	8.48×10^9	5.0
70 mm	8.79×10^9	8.8
75 mm	9.04×10^9	11.9
80 mm	9.25×10^9	14.5
85 mm	9.42×10^9	16.6
90 mm	9.57×10^9	18.4
Narrowing of the connection guide		
(60 → 60 mm) × 60 mm	8.51×10^9	0
(60 → 55 mm) × 60 mm	8.54×10^9	0.4
(60 → 50 mm) × 60 mm	8.38×10^9	−1.4
Guide type		
Cu/Ti - $m = 2.0$	8.08×10^9	0

Optimized parameter	**Intensity in analyzed area [n/s]**	**Gain [%]**
Ni/Ti - $m = 2.0$	8.27×10^9	2.4
Ni/Ti - $m = 2.5$	8.51×10^9	5.3
Ni/Ti - $m = 3.0$	8.51×10^9	5.3
Broadening after the pump slits		
Default - 2 mm	8.08×10^9	0
No broadening	8.33×10^9	3.1

Chapter 6

Performance Estimation

As the "PERC-template" contains the chopper, position and time sensitive evaluations of the neutron density can be performed. This chapter describes the propagation of a neutron pulse in the decay volume by monitoring the pulse at different times. Then, simulations of the magnetic field strength are combined with the time resolved neutron pulse simulations to analyze the magnetic mirror effect for beta asymmetry measurements. To complete the chapter, the estimated average decay rate of PERC will be calculated and compared to PERKEO III.

6.1 Neutron Pulse

When including the chopper in the simulations and using a position and time sensitive monitor called "PSD_TOF_monitor", time-of-flight information can be obtained. For this purpose, a monitor is positioned every 20 cm from $z = -0.4\,\mathrm{m}$ to $z = 8.8\,\mathrm{m}$ in the "PERC-template", making it possible to determine the position- as well as the time-dependent intensity of the neutron pulse in the central $50\,\mathrm{mm} \times 50\,\mathrm{mm}$. Figure 6.1 shows the relative intensity for a neutron pulse with $\lambda = 5\,\text{Å}$ at different positions in PERC. Note that the simulation uses the setup described in section 4.2, which does not include any of the optimizations described in chapter 5. Figure 6.2, shows the time-dependent relative intensity. This can be used to describe the magnetic mirror effect, which will be explained in section 6.2.

The velocity selector has a limited resolution. Therefore, at a frequency of the selector corresponding to $\lambda_{\mathrm{mean}} = 5\,\text{Å}$, the neutrons have a velocity between $v_{\mathrm{min}} = 720\,\frac{\mathrm{m}}{\mathrm{s}}$ and $v_{\mathrm{max}} = 880\,\frac{\mathrm{m}}{\mathrm{s}}$. This means that the neutron beam expands while it propagates in PERC. A visualization of this can be seen in figure 6.3, where the pulse shape at the beginning of PERC is compared to the pulse shape at the end of PERC. One can see that the length of the pulse increases significantly. Furthermore, neutrons with a selected wavelength of $\lambda = 5\,\text{Å}$ have a mean velocity of $v = 792\,\frac{\mathrm{m}}{\mathrm{s}}$. Hence $\Delta v_{\mathrm{max}} > \Delta v_{\mathrm{min}}$, which means that the fastest neutrons move away from the average faster than the slowest neutrons. That leads to a distortion of the pulse shape. A

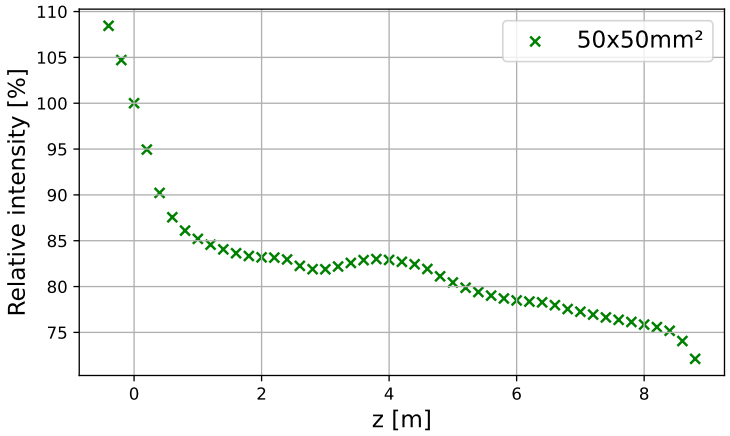

Figure 6.1: Relative neutron intensity in the inner 50 mm × 50 mm for the setup described in section 4.2. The average wavelength of the neutrons is 5 Å. The intensity is normalized to the intensity at the entrance of the decay volume. The beginning of PERC is located at $z = 0$ m. The neutron guide ends at $z = 8$ m. The gap effect fades after approximately 3 m leading to a slight intensity increase in the monitored area.

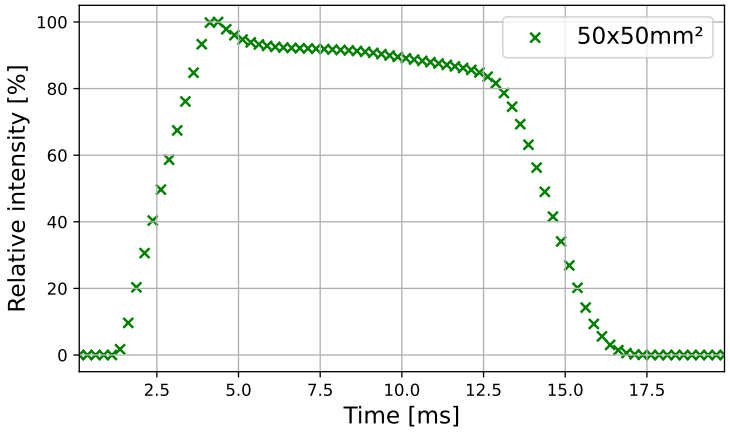

Figure 6.2: Time-dependent relative neutron intensity when monitoring the inner 50 mm × 50 mm and the length from $z = -0.4$ m to $z = 8.8$ m. The intensity is the sum over all detectors at the distinct time. It is normalized to the maximum value. At $t = 0$ ms the chopper opens. The average wavelength of the neutrons is 5 Å. As the chopper is open for a certain time period, the intensity increases in the beginning since more neutrons enter the decay volume. The decrease in the end is caused by the neutrons being absorbed by the beamstop.

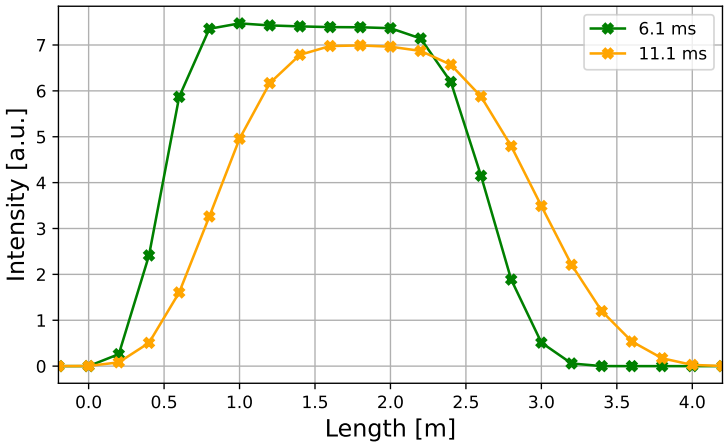

Figure 6.3: Comparison of the spatial distribution of a single pulse in PERC at two different times. The green line shows the pulse at the beginning of PERC with relative sharp edges. The orange line shows the same pulse at the end of the neutron guide before hitting the beamstop. The pulse has expanded and the edges softened due to the varying velocities of the neutrons inside a pulse.

full propagation of a single neutron pulse in the decay volume is shown in figure 6.4.

6.2 Magnetic Mirror Effect

In PERC, the neutrons decay in a magnetic field. As the electron and proton are charged particles, the Lorentz force influences them. Therefore, the charged decay products move helically along the magnetic field lines, with a gyration radius r

$$\boldsymbol{r} = \frac{m\boldsymbol{v}_\perp}{qB} = \frac{\boldsymbol{p}_\perp}{qB}, \tag{6.1}$$

where m is the mass of the decay particle, q is its charge and B is the magnetic field strength. $p_\perp$ is the perpendicular momentum, which can be determined by $p_\perp = p\sin(\theta)$, where θ is the emission angle relative to the z-axis, which is parallel to the magnetic field lines in the uniform decay volume. Assuming an adiabatic motion in PERC [12], the magnetic moment of the particle gyration μ is invariant, meaning that

$$\mu = \frac{mv_\perp^2}{2B} = \text{const.} \tag{6.2}$$

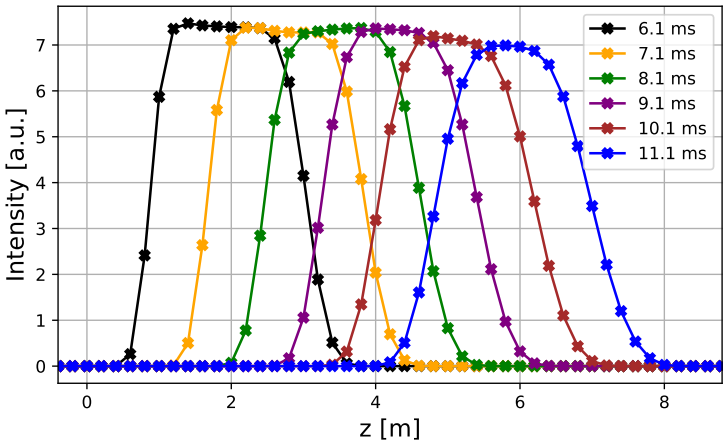

Figure 6.4: Propagation of a single neutron pulse through the decay volume of PERC. The beginning of PERC is located at $z = 0\,\mathrm{m}$. The neutron guide ends at $z = 8\,\mathrm{m}$. The pulse length expands as the neutrons have varying velocities due to the limited resolution of the velocity selector. The average neutron wavelength is 5 Å.

This results in the conservation of angular momentum and a constant ratio between the magnetic field and the squared perpendicular momentum of the decay particle

$$\boldsymbol{L} = \boldsymbol{r} \times \boldsymbol{p} = \text{const}, \quad \frac{p_\perp^2}{B} = \text{const}. \tag{6.3}$$

Furthermore, the energy of the particle is conserved

$$p^2 = p_\perp^2 + p_\parallel^2 = \text{const}, \tag{6.4}$$

where $p_\parallel$ is the momentum along the z-axis that determines the propagation velocity. $p_\parallel$ and $p_\perp$ are determined by the initial momentum and the angle θ to the z-axis, resulting from the neutron decay. In PERC, the magnetic field is not uniform. However, as derived, the fraction $\frac{p_\perp^2}{B}$ is constant. According to equation (6.4), that means that the longitudinal momentum transfers into transversal momentum with an increasing magnetic field, thereby decreasing the propagation velocity of the charged decay particle. In the region of the magnetic filter of PERC, there is a significant increase in the magnetic field. This can result in the longitudinal momentum decreasing to zero. In such a case, the decay particle is not able to pass the magnetic filter and will be reflected by the magnetic field. The transversal momentum decreases and the longitudinal momentum increases again, but the direction of the propagation has changed. A visualization of this is shown in figure 6.5. The particle can be detected by the upstream detector instead of the downstream detector. This influences the

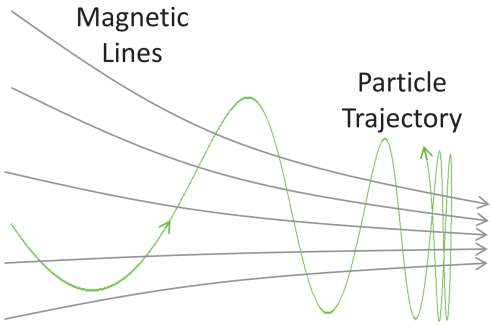

Figure 6.5: Sketch of the magnetic mirror effect due to an increasing magnetic field. Image is taken from [41].

number of particles reaching the up- and downstream detectors. As the momenta are determined by the angle θ, a critical angle for which the decay particles are able to reach the downstream detector can be defined. From equation (6.3) follows that

$$\frac{\sin^2\theta}{B} = \text{const}, \quad \sin\theta_2 = \sqrt{\frac{B_2}{B_1}}\sin\theta_1. \tag{6.5}$$

A charged particle cannot pass the magnetic filter if the angle to the z-axis increases to $\theta_1 = 90°$. Therefore, the critical angle θ_{crit} at any point in the decay volume can be determined by

$$\theta_{\text{crit}}(z) = \arcsin\left(\sqrt{\frac{B(z)}{B_{\text{filter}}}}\right). \tag{6.6}$$

Note that the critical angle usually depends on $\boldsymbol{r}$. However, a simulation of the magnetic field in PERC showed that the deviation in x- and y-direction is two orders of magnitude smaller than in z-direction, therefore it is negligible and $\boldsymbol{r}$ can be replaced by z.
Only the charged decay particles with an emission angle lower than the critical angle will be able to pass the magnetic filter. This changes the solid angle Ω of the particles that reach the main detector. It is given by

$$\Omega(z) = 2\pi(1 - \cos\theta_{\text{crit}}(z)). \tag{6.7}$$

As established previously, the magnetic field within PERC is not uniform. Hence, the critical angle depends on the location of the neutron decay. Due to the movement of the neutron pulse, this results in a time-dependent change of the measured decay rates.

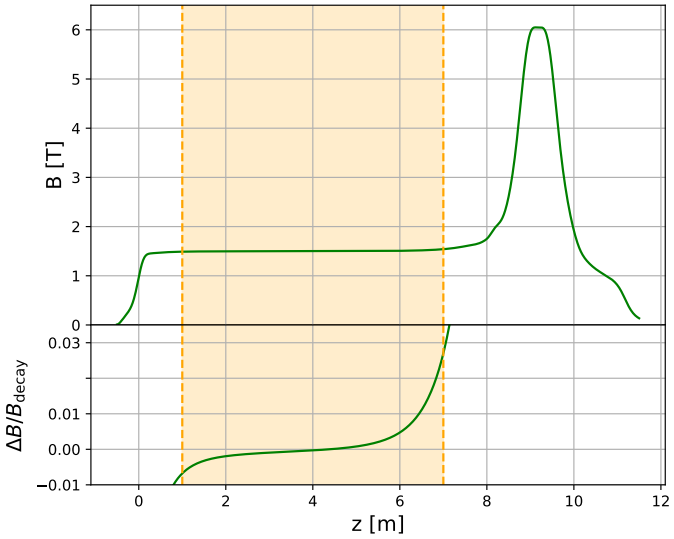

Figure 6.6: Magnetic field inside PERC for a configuration with $B_{\text{decay}} = 1.5\,\text{T}$ and $B_{\text{filter}} = 6\,\text{T}$. The beginning of PERC and the beginning of the superconducting magnet are located at 0 m. The highlighted area shows the part of the decay volume in which the magnetic field is considered uniform. The relative variation to the desired magnetic field of $B_{\text{decay}} = 1.5\,\text{T}$ is shown in the bottom part.

For a setup with $B_{\text{decay}} = 1.5\,\text{T}$ and a magnetic filter with $B_{\text{filter}} = 6\,\text{T}$, simulated data for the magnetic field is available [42]. A visualization of it is shown in figure 6.6. The deviations in x- and y-direction in the inner $60\,\text{mm} \times 60\,\text{mm}$ are negligible.

With knowledge of the magnetic field and equation (6.6), it is possible to calculate the critical angle in regard to the z-position. The result is shown in figure 6.7. Note that the critical angle depends on the ratio between the magnetic fields B_{decay} and B_{filter}, hence the critical angle changes significantly for different ratios.

As mentioned in section 2.4, the experimental beta asymmetry can be determined by the rates of electrons that are emitted parallel and antiparallel to the neutron spin. The decay rate of a point source can be determined by integrating the e^-/p^+-angular distribution, which is given by

$$W(\theta, E_e) = 1 + A^* \cos\theta. \tag{6.8}$$

A^* is an angular correlation signal, which is given by $A^* = \frac{v_\text{e}}{c} A P_\text{n}$ for the β-decay asymmetry A [12] . v_e is the electron velocity, c is the speed of light and P_n is the

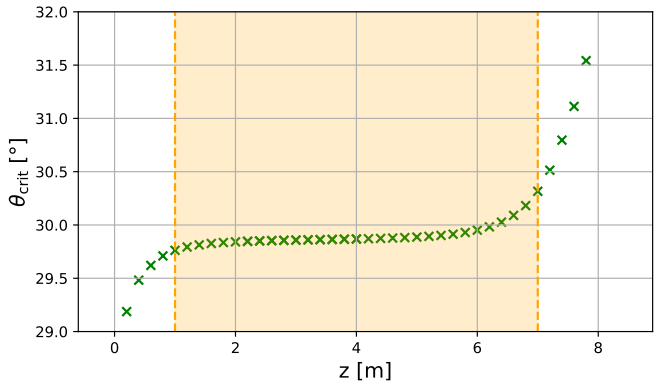

Figure 6.7: Critical angle of the magnetic mirror effect in regard to the decay position for a setup with $B_{\text{decay}} = 1.5\,\text{T}$ and $B_{\text{filter}} = 6\,\text{T}$. The beginning of PERC and the beginning of the superconducting magnet are located at 0 m. The highlighted area shows the part of the decay volume in which the magnetic field is considered uniform. Along the z-axis, the critical angle increases, which causes an increase in the measured decay rate at the downstream detector as more decay particles can pass the magnetic filter.

neutron polarization. The count rates of a point source for neutron spins parallel and antiparallel to the magnetic field are then given by

$$N^{\uparrow}_{\text{p,src}}(E_e) = \int_0^{\theta_{\text{crit}}} W(\theta, E_e) \sin\theta d\theta \quad \text{and} \quad N^{\downarrow}_{\text{p,src}}(E_e) = \int_{\pi-\theta_{\text{crit}}}^{\pi} W(\theta, E_e) \sin\theta d\theta. \tag{6.9}$$

Note that the emission angle of the decay particle, which determines the interval limits, is in regard to the neutron spin axis. Therefore, for parallel and antiparallel spin orientation different emission angles are covered by the solid angle that is detected by the downstream detector. As the neutron pulse in PERC has a time-dependent spatial distribution, it is not a point source. Hence, one has to integrate over all point sources in the decay volume, considering the neutron density $\rho(\boldsymbol{r}, t)$. The decay rates are then given by

$$N^{\uparrow}(E_e, t) = \int_V N^{\uparrow}_{\text{p,src}}(E_e)\rho(\boldsymbol{r}, t)\mathrm{d}^3\boldsymbol{r} \quad \text{and} \quad N^{\downarrow}(E_e, t) = \int_V N^{\downarrow}_{\text{p,src}}(E_e)\rho(\boldsymbol{r}, t)\mathrm{d}^3\boldsymbol{r}. \tag{6.10}$$

As the deviations in x- and y-direction are negligible, the volume integral can be replaced with an integral over z by introducing an area density $\rho(z, t)$. The numerator

$N^{\uparrow}(E_e,t)-N^{\downarrow}(E_e,t)$ and the denominator $N^{\uparrow}(E_e,t)+N^{\downarrow}(E_e,t)$ of the experimental beta asymmetry in equation (2.8) are then given by

$$\begin{aligned} N^{\uparrow}(E_e,t) - N^{\downarrow}(E_e,t) &= A^* \int_z \rho(z,t)\frac{B(z)}{B_{\text{filter}}}\mathrm{d}z \\ N^{\uparrow}(E_e,t) + N^{\downarrow}(E_e,t) &= 2\left(\int_z \rho(z,t)\mathrm{d}z - \int_z \rho(z,t)\cos\theta_{\text{crit}}(z)\mathrm{d}z\right). \end{aligned} \tag{6.11}$$

Combining equation (2.8) with these results gives the description of the measured experimental beta asymmetry as a function of time.

As the magnetic mirror effect influences the measured asymmetry, one needs the from now on so-called magnetic mirror factor F_{MM} to calculate the beta asymmetry. With the time resolved neutron beam simulation from section 6.1, this factor can be determined. The simulation provides the area density $\rho(z,t)$ for distinct times and positions, hence the integral over the continuous beam can be exchanged by a sum. The magnetic mirror factor is then given by

$$F_{\text{MM}}(t) = \frac{\sum_z \rho(z,t)\frac{B(z)}{B_{\text{filter}}}}{\sum_z \rho(z,t) - \sum_z \rho(z,t)\cos\theta_{\text{crit}}(z)}. \tag{6.12}$$

For the magnetic field in figure 6.6, the time-dependent magnetic mirror factor is shown in figure 6.8. The ratio $\frac{\Delta F_{\text{MM}}}{F_{\text{MM}}}$ changes within the measured time period by approximately 2×10^{-4}, resulting in a fractional change $\frac{\Delta A_{\text{MM}}}{A}$ on the beta asymmetry caused by the magnetic mirror effect. The effect is one order of magnitude smaller than for PERKEO III [10]. On average, the effect largely cancels out due to the approximately linear slope. Therefore, the uncertainty should be significantly lower, making it only a minor error source for the projected uncertainty of $\frac{\Delta A}{A} = 5\times10^{-4}$.

As the magnetic field in the decay volume and the area of the magnetic filter are maintained by different power supplies, it is of interest to check the effect of a change in the magnetic field strength. To analyze this, a deviation of 10^{-3} of B_{filter} is considered. The results of such a deviation on the magnetic mirror factor are shown in figure 6.9. With a deviation of 10^{-3}, the magnetic mirror factor changes by approximately 10^{-4}. This is in accordance with the PERC paper [12] and shows that the ratio $\frac{B_{\text{decay}}}{B_{\text{filter}}}$ must be known with a precision of 10^{-3}. As the monitoring of the magnetic field will be done with a precision of 10^{-4} or better, this causes no problems.

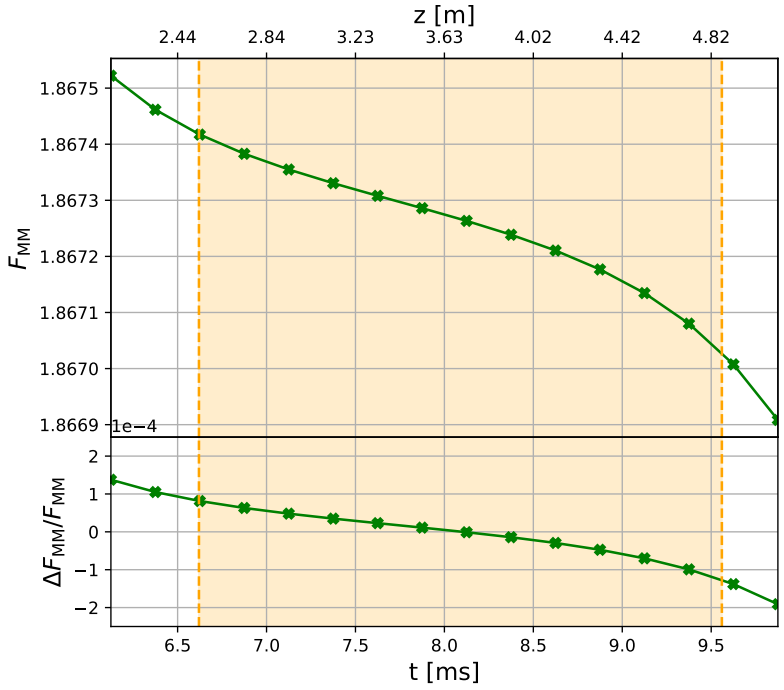

Figure 6.8: Magnetic mirror factor as a function of time for a magnetic field with $B_{\text{decay}} = 1.5\,\text{T}$ and $B_{\text{filter}} = 6\,\text{T}$. The highlighted area shows the time period of the measurement t_{meas}. The second x-axis shows the position of a neutron with $\lambda = 5\,\text{Å}$ that passed the chopper at $t = \frac{t_{\text{open}}}{2}$. The beginning of PERC is located at $z = 0\,\text{m}$.

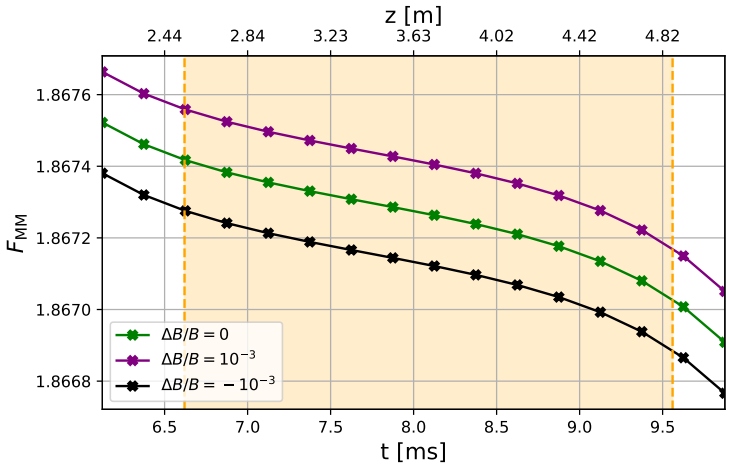

Figure 6.9: Magnetic mirror factor as a function of time. The purple and the black line show the magnetic mirror factor if the field strength deviates by $\pm 6 \times 10^{-3}\,\mathrm{T}$. The highlighted area shows the time period of the measurement t_{meas}. The second x-axis shows the position of a neutron with the average wavelength that passed the chopper at $t = \frac{t_{\mathrm{open}}}{2}$. The beginning of PERC is located at $z = 0\,\mathrm{m}$.

6.3 Decay Rate Estimate

In section 5.2 the average particle flux densities for different setups without chopper and polarizer were determined. With the averaged unpolarized particle flux density ϕ, a decay rate estimate can be done. As the simulations were performed without a polarizer, its transmission needs to be considered separately. However, it has not been decided yet which type of polarizer will be used, hence the transmission T_{pol} can only be approximated. In the following calculations, it is assumed to be $T_{\mathrm{pol}} = 0.3$. The polarized flux density is then given by

$$\phi_{\mathrm{pol}} = T_{\mathrm{pol}}\phi. \tag{6.13}$$

To determine the instantaneous decay rate r_{inst}, the number of neutrons in the decay volume (here equivalent to the number of neutrons in a single pulse) must be divided by the neutron lifetime. The number of neutrons in the decay volume is given by the product of the polarized flux density with the usable beam cross section A, the time the chopper is open and factor F_{ideal} to consider the chopper opening function. The instantaneous decay rate for polarized neutrons is then given by

$$r_{\mathrm{inst}} = \frac{A\phi_{\mathrm{pol}}F_{\mathrm{ideal}}t_{\mathrm{open}}}{\tau_{\mathrm{n}}}. \tag{6.14}$$

Since the neutron pulses are not constantly inside the uniform magnetic field, one can only measure during a fraction of the available time. Therefore, an average decay rate r_{avg} must be determined. It is given by

$$r_{\mathrm{avg}} = r_{\mathrm{inst}} f_{\mathrm{chop}} t_{\mathrm{meas}}. \tag{6.15}$$

For the setup described in section 4.2, the unpolarised particle flux density is approximately $\phi = 2.63 \times 10^8\,\mathrm{cm^{-2}s^{-1}}$. With an observed cross section of $50\,\mathrm{mm} \times 50\,\mathrm{mm}$ and the parameters for $\lambda = 5\,\text{Å}$ from table 3.1, the observable instantaneous decay rate in PERC is $r_{\mathrm{inst}} = 6.1 \times 10^3\,\mathrm{s^{-1}}$. That results in an average decay rate of $r_{\mathrm{avg}} = 882\,\mathrm{s^{-1}}$.

To compare this to the average event rate in PERKEO III, one has to consider the conceptual changes. At PERKEO III, the asymmetry measurement was done with one detector at each end and without a magnetic filter. At PERC, only the downstream detector will be used for the asymmetry measurement, which, in comparison, halves the detected decay rate. Furthermore, due to the magnetic filter, only a fraction of the decay particles reach the downstream detector. The transmission of the filter is described by $T_{\mathrm{filter}} = 1 - \cos\theta_{\mathrm{crit}}$, which can be derived from equation (6.7). However, as described by equation (2.9), the asymmetry is enhanced by a factor

$A_{\text{filter}} = 1 + \cos\theta_{\text{crit}}$. Therefore, the comparable event rate to PERKEO III is given by

$$r_{\text{avg,comp}} = \frac{1}{2} r_{\text{avg}} A_{\text{filter}} T_{\text{filter}}. \tag{6.16}$$

The resulting event rate is $r_{\text{avg,comp}} = 110\,\text{s}^{-1}$. That is similar to the rate at PERKEO III [29]. Although PERC has significantly improved systematics one also wants better statistics, which shows why optimizations are necessary. This event rate does not include any of the optimizations to the average neutron intensity. It was found that the average neutron intensity could be increased by approximately 90 %. As this is directly proportional to the decay rates, the same is true for those. Furthermore, it was mentioned in section 3.6 that changing the approach of the background measurement could increase the chopper frequency by up to 86 %. Therefore, depending on the chosen adaptions, the average event rate could be increased to up to $r_{\text{avg,comp}} = 400\,\text{s}^{-1}$. The PERC paper [12] assumes an average event rate of $9 \times 10^4\,\text{s}^{-1}$ for an unpolarized continuous neutron beam. This translates to a rate of $r_{\text{avg,comp}} \approx 360\,\text{s}^{-1}$ for a polarized pulsed beam. When including the optimizations this rate can be realized.

Note that, as with all the other simulations, there is no statistical uncertainty given as 10^{10} neutrons were simulated. The accuracy is systematically limited by the approximations their uncertainties.

Chapter 7

Conclusion and Outlook

With PERC, the successor of PERKEO III, being prepared for first measurements in the near future, more precise results for the Fierz interference term b, the beta asymmetry A and other decay coefficients lie ahead. As the start of operation approaches, it is necessary to develop a chopper, which is optimized for the use in PERC.

To optimize the chopper disc, a versatile template was created that can account for different neutron wavelengths, guide cross sections and distances. With the template it is also possible to analyze the chopper opening function, which helps to decide whether to use a single disc chopper or a two disc counter-rotating chopper. It was found that at $\lambda = 5\,\text{Å}$, if the background measurement is included in the pulse cycle, a single disc chopper is the most reasonable option. At this wavelength an absorber thickness of 1 mm of boron carbide was found sufficient to obtain a transmission of $T \ll 10^{-5}$. The template can account for a changed wavelength of the incoming neutrons and recalculates all results. The energy content and tensile stresses of the disc are calculated. At the desired radius of r_{ges}, the tensile stress is calculated to be 13.9 MPa at a frequency of $f_{\text{chop}} = 50\,\text{Hz}$, which verifies that a chopper made out of boron carbide and reinforced polyimid is safe for operation. Additionally, an approach without background measurement in the pulse cycle was proposed, highlighting also necessary changes to the concept. This approach would increase the average event rate by up to 86 % but requires a two-window chopper disc to prevent frequencies close to 100 Hz.

Using the Python-API McStasScript, a "PERC-template" for neutron simulations was developed. With the simulations, it was discovered that a gap in the guide causes an inhomogeneous intensity distribution inside the decay volume. Minimizing this effect was part of the optimization.

The average neutron density in PERC was analyzed in great detail and measures to increase the number of observed neutron decays were proposed. These suggestions include the use of neutrons with $\lambda = 4.5\,\text{Å}$ instead of 5 Å, as well as increasing height and width of the neutron guides, and using supermirrors with a higher m-value. By implementing all proposed changes, the average decay rate could be increased by up

to 90 %. This analysis is especially important because the cold source at the FRM II is currently unavailable, making PERC statistically limited until the cold source can be operated again. The "PERC-template" is already used by L. Löbell to compare the suitability of different types of polarizers for the use with PERC.

A time of flight analysis of the pulsed neutron beam was performed, enabling the calculation of the time dependent systematic effect of the magnetic mirror effect. It was found that the relative correction on the beta asymmetry caused by the magnetic mirror effect is approximately $\frac{\Delta A_{\mathrm{MM}}}{A} = 2 \times 10^{-4}$, which is an order of magnitude lower than for PERKEO III. Furthermore, the average decay rate was estimated. With the cold source and without changes to the beamline or the measurement approach, the measured decay rate is comparable to that of PERKEO III, resulting in similar statistics, while the systematics are significantly better with PERC. The decay rate is estimated to be $r_{\mathrm{avg,comp}} = 110\,\mathrm{s}^{-1}$ in a configuration with $B_{\mathrm{decay}} = 1.5\,\mathrm{T}$ and $B_{\mathrm{filter}} = 6\,\mathrm{T}$. Including the proposed changes could increase this rate to up to $r_{\mathrm{avg,comp}} = 400\,\mathrm{s}^{-1}$.

Additionally, it is currently being checked if tilting the velocity selector is an option to transmit neutrons of lower wavelengths that have a higher intensity in the source. First results predict a reachable neutron wavelength of $\lambda = 3\,\text{Å}$, while [12] assumes a resolution of $\frac{\Delta\lambda}{\lambda} = 20\,\%$. The wavelength spectrum from the FRM II shown in figure 5.11 has a maximum at around $\lambda = 3\,\text{Å}$, with its intensity being approximately 1.7 times higher than at $\lambda = 5\,\text{Å}$. Furthermore, a resolution of $\frac{\Delta\lambda}{\lambda} = 20\,\%$ approximately doubles the number of transmitted neutrons. Therefore, the statistics could be increased by an additional factor of up to 3.4, showing that the statistical potential is not yet utilized.

This and the feasibility study of some of the proposed optimizations is still ongoing. Especially increasing height and width of the neutron guides might be challenging. Once these analyses are finished, the parameters of the beamline have to be finalized. Since these decisions affect the geometry and rotation frequency of the chopper, the chopper layout must be adapted, taking into account the finalized parameters. All chopper calculations, the "PERC-template", the analysis of the magnetic mirror effect, and the decay rate estimation are done with adaptable scripts, so the calculations can easily be repeated. With the layout of the chopper finalized, the chopper can be mechanically designed and built to obtain an optimized pulsed neutron beam in PERC.

Appendix A

Additional Figures

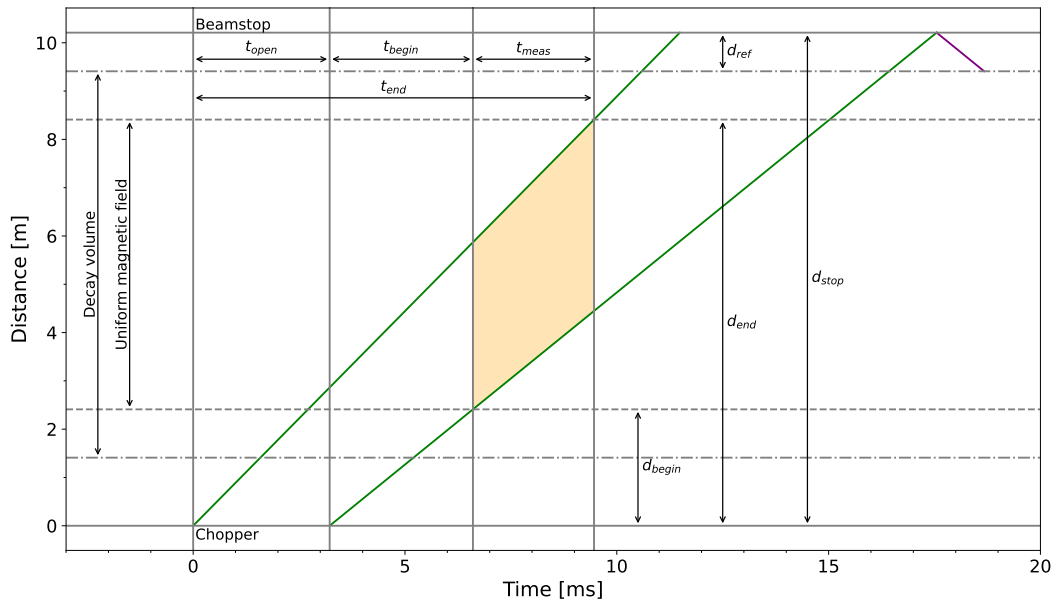

Figure A.1: Visualization of the distances and time periods that are necessary to optimize the chopper. The distances are given in relation to the chopper disc. The green lines delimit the neutron pulse in position and time.

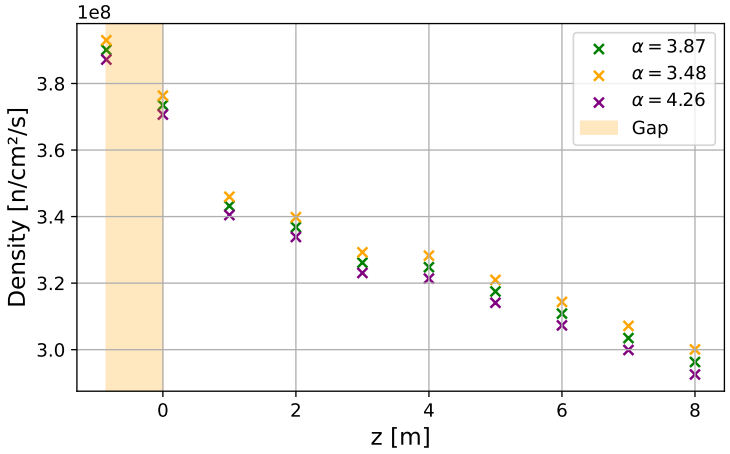

Figure A.2: Average neutron density for different α, which determines the slope of the reflectivity curve. The beginning of PERC is located at $z = 0\,\mathrm{m}$. As the supermirrors of the neutron guides are not produced yet, the reflectivity parameters might deviate from the estimates. If α changes by $10\,\%$, the average neutron density changes by $1\,\%$.

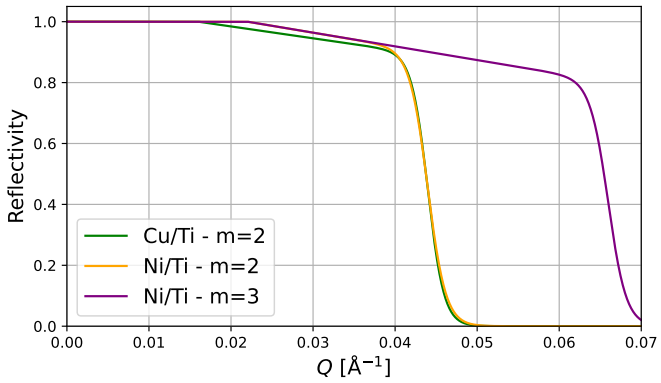

Figure A.3: Comparison of the reflectivity curves of an $m = 2$ Cu/Ti supermirror and Ni/Ti supermirrors with $m = 2$ and $m = 3$. The commercially available $m = 3$ Ni/Ti supermirror has a higher reflectivity, resulting in less neutron absorptions along the guide.

Bibliography

[1] Makoto Kobayashi and Toshihide Maskawa. »CP-Violation in the Renormalizable Theory of Weak Interaction«. In: *Progress of Theoretical Physics* 49.2 (Feb. 1973), pp. 652–657. ISSN: 0033-068X. DOI: 10.1143/PTP.49.652.

[2] Lincoln Wolfenstein. »Parametrization of the Kobayashi-Maskawa Matrix«. In: *Phys. Rev. Lett.* 51 (1983), pp. 1945–1947. DOI: 10.1103/PhysRevLett.51.1945.

[3] Y. Fukuda et al. »Evidence for Oscillation of Atmospheric Neutrinos«. In: *Physical Review Letters* 81.8 (Aug. 1998), pp. 1562–1567. ISSN: 0031-9007, 1079-7114. DOI: 10.1103/PhysRevLett.81.1562.

[4] F. Zwicky. »Die Rotverschiebung von extragalaktischen Nebeln«. In: *Helv. Phys. Acta* 6 (1933), pp. 110–127. DOI: 10.1007/s10714-008-0707-4.

[5] Matthew D. Schwartz. *Quantum Field Theory and the Standard Model*. Cambridge: Cambridge University Press, 2013.

[6] S. Navas et al. »Review of Particle Physics«. In: *Phys. Rev. D* 110.3 (2024), p. 030001. DOI: 10.1103/PhysRevD.110.030001.

[7] E. Fermi. »Versuch einer Theorie der β-Strahlen. I«. In: *Zeitschrift für Physik* 88.3-4 (Mar. 1934), pp. 161–177. ISSN: 1434-6001, 1434-601X. DOI: 10.1007/BF01351864.

[8] H. W. Wyld J. D. Jackson S. B. Treiman. »Possible Tests of Time Reversal Invariance in Beta Decay«. In: *Physical Review* 106.3 (1957), pp. 517–521. DOI: 10.1103/PhysRev.106.517.

[9] Karina Lisa-Marie Bernert. »Beta Spectroscopy in Neutron Decay«. PhD Thesis. Technical University of Munich, TUM School of Natural Sciences, 2025.

[10] Heiko Saul. »Energy Dependence of the Beta Asymmetry in Neutron Beta Decay«. PhD Thesis. 2018.

[11] Max Lamparth. »Fierz Interference Term in Neutron Beta Decay and New Approaches for Systematic Uncertainty Quantification«. PhD Thesis. Munich: Technische Universität München, 2023. URL: https://nbn-resolving.org/urn:nbn:de:bvb:91-diss-20230728-1714907-1-0.

[12] D. Dubbers et al. »A clean, bright, and versatile source of neutron decay products«. In: *Nuclear Instruments and Methods in Physics Research Section A: Accelerators, Spectrometers, Detectors and Associated Equipment* 596.2 (2008), pp. 238–247. ISSN: 0168-9002. DOI: https://doi.org/10.1016/j.nima.2008.07.157.

[13] D.H. Wilkinson. »Analysis of neutron β-decay«. In: *Nuclear Physics A* 377.2 (1982), pp. 474–504. ISSN: 0375-9474. DOI: https://doi.org/10.1016/0375-9474(82)90051-3. URL: https://www.sciencedirect.com/science/article/pii/0375947482900513.

[14] Dominik Werder. »Development and Characterization of a Pulsed Beam for Neutron Decay Experiments«. Diploma Thesis. Heidelberg: University of Heidelberg, Department of Physics and Astronomy, 2009.

[15] Glenn F. Knoll. *Radiation Detection and Measurement*. 4th ed. New York: John Wiley & Sons, 2010.

[16] Wolfgang Demtröder. *Experimentalphysik 4. Kern-, Teilchen- und Astrophysik*. 5th ed. Springer-Lehrbuch. Springer Spektrum Berlin, Heidelberg, 2017. DOI: 10.1007/978-3-662-52884-6.

[17] A. J. Dianoux and G. H. Lander, eds. *Neutron Data Booklet*. 2nd. Old City Publishing, 2003.

[18] P. J. J. Kok. *Capture of Thermal Neutrons in ^{10}B and ^{6}Li*. Tech. rep. Netherlands Energy Research Foundation, Petten, July 1986.

[19] Shigeaki Okajima, Teruhiko Kugo and Takamasa Mori. *Nuclear Reactor Physics*. 1st ed. Springer Tokyo, 2024. DOI: 10.1007/978-4-431-55600-8.

[20] Varley F. Sears. *Neutron Scattering Lengths and Cross Sections*. 1992.

[21] John R. Lamarsh and Anthony J. Baratta. *Introduction to Nuclear Engineering*. 3rd. Prentice Hall, 2001.

[22] Wolfgang Demtröder. *Experimentalphysik 1: Mechanik und Wärme*. 7th ed. Springer-Lehrbuch. Berlin, Heidelberg: Springer Spektrum, 2015. ISBN: 978-3-662-46414-4. DOI: 10.1007/978-3-662-46415-1. URL: https://link.springer.com/book/10.1007/978-3-662-46415-1.

[23] Laminated Plastics. *Technical Data Sheet: Polyimide*. 2013.

[24] Piaras Kelly. *Solid Mechanics Part II: Engineering Solid Mechanics*. University of Auckland, 2013.

[25] F. James. »Monte Carlo Theory and Practice«. In: *Reports on Progress in Physics* 43 (1980), p. 1150.

[26] P. Willendrup et al. *User and Programmers Guide to the Neutron Ray-Tracing Package McStas*. Manual. Physics Department, Technical University of Denmark. 2024.

[27] Mads Bertelsen. *McStasScript Documentation: Overview*. 2022.

[28] Alexander Hollering. »Development of neutron optical components for PERC«. PhD Thesis. Technische Universität München, 2022.

[29] *Private communication with Bastian Märkisch*. May 2025.

[30] V. Wagner H. Friedrich and P. Wille. »A high-performance neutron velocity selector«. In: *Physica B: Condensed Matter* 156-157 (1989), pp. 547–549. ISSN: 0921-4526. DOI: https://doi.org/10.1016/0921-4526(89)90727-8.

[31] Dornier GmbH Systems Technology. *Neutron Velocity Selector*. Manual.

[32] Alexander Petukhov et al. *A project of advanced solid-state neutron polarizer for PF1B instrument at ILL*. June 2019. DOI: 10.48550/arXiv.1906.04690.

[33] Stefan Bodmaier. »The vacuum pump system of PERC«. Master's Thesis. Technische Universität München, 2018.

[34] Christine Klauser. »High Precision Neutron Polarization For PERC«. PhD Thesis. Technische Universität Wien, Oct. 2013.

[35] John R. Taylor. *An Introduction to Error Analysis - The study of uncertainties in physical measurements*. 2nd ed. University Science Books, 1997.

[36] Varley F. Sears. *Neutron Optics: An Introduction to the Theory of Neutron Optical Phenomena and Their Applications*. Oxford University Press, 1989.

[37] C Schanzer, M. Schneider and P Böni. »Neutron Optics: Towards Applications for Hot Neutrons«. In: *Journal of Physics: Conference Series* 746 (Sept. 2016), p. 012024. DOI: 10.1088/1742-6596/746/1/012024.

[38] P. Willendrup et al. *Component Manual for the Neutron Ray-Tracing Package McStas, version 3.5*. Physics Department, Technical University of Denmark. 2800 Kongens Lyngby, Denmark, Aug. 2024.

[39] G. L. Squires. *Introduction to the Theory of Thermal Neutron Scattering*. 3rd ed. Cambridge University Press, 2012.

[40] SwissNeutronics AG. *Neutron Supermirrors*. (visited on 24/04/2025). 2025. URL: https://www.swissneutronics.ch/products/neutron-supermirrors/.

[41] Xiangzun Wang. »The Free Neutron -Decay: A Powerful Tool for the Investigation in Particle Physics«. PhD Thesis. Munich: Technische Universität München, Mar. 2013.

[42] *Private communication with Karina Bernert*. May 2025.